

# Micro-Mechanics of Re-entrant Hexagonal Auxetic Structures and Its Blast Resistance

Rajesh Kumar Meena

A Thesis Submitted to  
Indian Institute of Technology Hyderabad  
In Partial Fulfillment of the Requirements for  
The Degree of Master of Technology

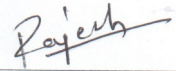


Department of Mechanical and Aerospace Engineering

July 2015

## Declaration

I declare that this written submission represents my ideas in my own words, and where ideas or words of others have been included, I have adequately cited and referenced the original sources. I also declare that I have adhered to all principles of academic honesty and integrity and have not misrepresented or fabricated or falsified any idea/data/fact/source in my submission. I understand that any violation of the above will be a cause for disciplinary action by the Institute and can also evoke penal action from the sources that have thus not been properly cited, or from whom proper permission has not been taken when needed.



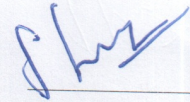
(Signature)

Rajesh Kumar Meena  
(Student name)

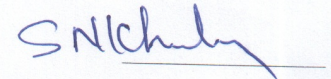
ME10B14M000004  
(Roll No.)

## Approval Sheet

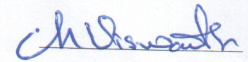
This Thesis entitled Micro-Mechanics of Re-entrant Hexagonal Auxetic Structures and Its Blast Resistance by Rajesh Kumar Meena is approved for the degree of Master of Technology from IIT Hyderabad



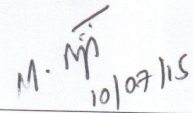
(Dr. S. Suriya Prakash) Examiner  
Assistant Professor  
Department of Civil Engineering  
Indian Institute of Technology, Hyderabad



(Dr. Syed Nizamuddin Khaderi) Examiner  
Assistant Professor  
Department of Mechanical and Aerospace Engineering  
Indian Institute of Technology, Hyderabad



(Dr. Viswanath Chinthapenta) Advisor  
Assistant Professor  
Department of Mechanical and Aerospace Engineering  
Indian Institute of Technology, Hyderabad



(Dr. Ramji M) Chairman  
Associate Professor  
Department of Mechanical and Aerospace Engineering  
Indian Institute of Technology, Hyderabad

## Acknowledgements

First and foremost, I would like to express my deepest gratitude to my advisor, Dr. Viswanath Chinthapenta, for his excellent guidance, caring and patience. I would like to thank both Prof. S. Gopala krishnan and Dr. Viswanath for introducing me to this topic. I would like to thank my defense committee Dr. M Ramji, Dr. Syed Khaderi Nizamuddin, Dr. Gangadharan and Dr. Suriya for their valuable comment and suggestions. I would like to thank my peers Mr. Pratap rao, Mr. Harilal, Mr. Sammed, Mr. Yagnik and Mr. Jis tom for the helpful research discussions. And, I would like to thank my friends for the good time I had in last five years. Special thanks goes to my parents Mr. Nana singh and Mrs. Geeta devi for getting me started on my journey, providing me the opportunity for a great education, and giving me the freedom to choose my path.

# Dedication

To my beloved family

## Abstract

Auxetics are mechanical meta-materials which exhibit negative Poisson's ratio. In here, first study is focused on blast resistance of sandwich beams with an auxetic core having re-entrant hexagonal topology. We implemented the Fleck and Deshpande's three stage momentum transfer model to estimate the dynamic structural response of auxetic cored sandwich beams. The mechanical behavior of auxetic core such as normal compressive strength  $\sigma_{ny}$  and the longitudinal strength  $\sigma_{ly}$  are required for the above mentioned three stage modelling of sandwich beams. Hence, the objective of our study is to investigate the mechanical behaviors of auxetic material for various geometric configurations using finite element simulations. We performed Monte Carlo study to obtain the mechanical properties using micro-structural parameters. Using the  $\sigma_{ny}$  and  $\sigma_{ly}$  obtained from the static FE simulations we studies the blast resistance of the auxetic cores. We observed that the auxetic core outperforms the other conventional core structures. During this process the computational efforts were high because auxetic has a re-entrant corner so we further continued this study to develop an enriched element. We have developed an analytical formulation for configurational force using Ashby's beam column method. We attempted to enrich a 4-noded rectangular element for an hourglass structure using the corner singularities based on the concept of extended finite element methods.

# Contents

Acknowledgements . . . . .	iv
Abstract . . . . .	vi
<b>Nomenclature</b>	<b>viii</b>
<b>1 Introduction</b>	<b>5</b>
1.1 Poisson's Ratio . . . . .	5
1.2 Auxetic Materials . . . . .	6
1.3 Re-entrant Honeycomb Auxetics . . . . .	10
1.4 Blast and Plane Shock-wave Propagation . . . . .	11
1.5 Sandwich Beams . . . . .	14
1.6 Blast resistance of Sandwich beams . . . . .	15
<b>2 Blast Resistance of Sandwich Beam Comprising Auxetic Core</b>	<b>17</b>
2.1 Motivation of Study . . . . .	17
2.2 Introduction . . . . .	18
2.3 Methodology . . . . .	19
2.3.1 Representative Unit Cell Homogenization . . . . .	19
2.3.2 Finite Element Modelling . . . . .	21
2.3.3 Mesh convergence study . . . . .	21
2.3.4 Three Stage Momentum Transfer model . . . . .	24
<b>3 Results and Discussions: Blast Resistance of Sandwich Beams Comprising Auxetic Core</b>	<b>28</b>
3.1 Mechanical Properties of Re-entrant Honeycomb . . . . .	28
3.2 Performance Charts for Under Water Blast Resistance . . . . .	29
<b>4 Mechanics of Re-entrant Hexagonal Honeycomb</b>	<b>35</b>
4.1 Introduction . . . . .	35
4.2 In-plane Properties of Re-entrant Hexagon: Uni-axial loading . . . . .	36
4.2.1 Linear Elastic Deformation . . . . .	37
4.2.2 Plastic Collapse . . . . .	40
4.3 Corner Singularity of Re-entrant Wedge . . . . .	42
4.4 Direct stiffness methods using frame element . . . . .	44
4.5 Configuration Forces in Re-entrant Hexagonal Auxetic . . . . .	46

<b>5</b>	<b>Result and Discussions: Mechanics of Re-entrant Hexagonal Honeycomb</b>	<b>49</b>
5.1	In plane properties of re-entrant hexagonal structure . . . . .	49
5.2	Corner Singularity of Re-entrant Wedge . . . . .	53
5.3	Direct Stiffness Method using frame element . . . . .	55
5.4	Configurational Forces in Re-entrant Hexagonal Auxetic . . . . .	57
<b>6</b>	<b>Conclusion and Future Scope</b>	<b>59</b>
6.0.1	Key Conclusion . . . . .	59
6.0.2	Future Scope . . . . .	59
<b>A</b>	<b>Analytical Three Stage Momentum Transfer Model</b>	<b>61</b>
A.1	Model Description . . . . .	61
A.1.1	Stage I: One Dimensional Fluid-Structure Interaction Model. . . . .	61
A.1.2	Stage II: One Dimensional Model of Core Compression Phase . . . . .	62
A.1.3	Stage III: Dynamic Structural Response of Clamped Sandwich Beam . . . . .	63
	<b>References</b>	<b>66</b>



# List of Figures

1.1	Poisson's effect on a conventional material when load is applied in x direction. . . . .	5
1.2	Schematic of negative Poisson's ratio effect on 2D shape . . . . .	6
1.3	Geometries exhibiting Auxetic behavior [1]. (a) Re-entrant hexagon (b) Chiral square symmetric [2] (c) Chiral circular [2] (d) Rotating unit squares [3] . . . . .	7
1.4	Distortion behavior of surface a) Anticlastic surface b) Synclastic surface [4] . . . . .	7
1.5	Re-entrant unit cell produced by symmetric collapse [5] . . . . .	9
1.6	Auxetic foam by 3D printing Critchley et al. [6] . . . . .	10
1.7	liquid crystalline polymer (LCP) (a) undeformed, and (b) deformed states [1] . . . . .	10
1.8	Schematic of re-entrant hexagonal auxetic . . . . .	11
1.9	Deformation mechanism of honeycomb cores: (a) Re-entrant hexagon (b) Regular hexagon. . . . .	12
1.10	Phenomenons involved in the energy release due to an explosion. . . . .	12
1.11	Shockwave propagation in water . . . . .	13
1.12	Sandwich beam . . . . .	14
1.13	Sandwich beam core topologies [1]. . . . .	14
2.1	Material flow direction on indentation (a) Non-auxetics material (b) Auxetic materials [7]. . . . .	18
2.2	Geometric parameters of representative unit cell . . . . .	20
2.3	Representative unit cell of re-entrant honeycombs. Elements with red boundary have been chosen for homogenization. . . . .	20
2.4	Re-entrant hexagon model . . . . .	22
2.5	Loading and Boundary conditions . . . . .	22
2.6	Re-entrant model mesh with 6 element across the cell rib thickness and zoomed view	23
2.7	Mesh convergence curve for re-entrant hexagon model . . . . .	24
2.8	Threes stages of dynamic response of sandwich beam to impulse (a) Stage-I b) Stage-II (c) Stage-III . . . . .	26
2.9	Sandwich beam geometry . . . . .	27
3.1	Schematic : Plot between $\ln(\frac{\sigma_{ly}}{\sigma_y})$ vs $\ln \bar{\rho}$ . . . . .	28
3.2	Data points obtained from the Monte Carlo analysis using finite element simulations of auxetic lattice structure. . . . .	29

3.3	Normalized time response $\bar{T}$ and normalized deflection $\bar{w}$ of inner face of sandwich beam ( $\bar{c}=0.1, \bar{h}=0.1$ ) with auxetic core ( $\bar{\rho}=0.1, \epsilon=0.002, \epsilon_D=0.5$ ) w.r.t. to normalized impulse $\bar{I}$ for . . . . .	30
3.4	Tensile strain $\epsilon_m$ and tensile strain of beam ( $\bar{c}=0.1, \bar{h}=0.1$ ) with auxetic core ( $\bar{\rho}=0.1, \epsilon=0.002, \epsilon_D=0.5$ ) w.r.t. to normalized impulse $\bar{I}$ . . . . .	31
3.5	Design chart including contours of $\bar{w}$ and $\epsilon_c$ for a sandwich beam with an auxetic core of parameters $\bar{\rho}=0.1, 0.002, \epsilon=0.5$ , subjected to a water blast ( $\bar{I} = 10^{-2}$ and $\bar{\psi} = 2e^3$ )	32
3.6	The tensile failure regime variation with respect to non-dimensional fluid structure interaction parameter $\bar{\psi}$ for sandwich beam with auxetic core ( $\bar{\rho}=0.1, \epsilon_y=0.002, \epsilon_D=0.5$ ) under $\bar{I} = 10^{-2}$ . . . . .	32
3.7	Comparison between re-entrant hexagonal auxetic core and Hexagonal core in terms of variation tensile failure regime with respect to non-dimensional fluid structure interaction parameter $\bar{\psi}$ . . . . .	33
3.8	Inverse design chart for a sandwich beam, with a re-entrant hexagonal auxetic core ( $\bar{\rho}=0.1, \epsilon_y=0.002, \epsilon_D=0.5$ , subjected to a water blast. The beam deflection is $\bar{w}=0.1$ and the fluid-structure interaction parameter is taken as $\psi = 2X10^{-3}$ . Contours of $\bar{T}$ and $\bar{M}$ are displayed. The dotted lines trace the paths of selected values of $\frac{h}{L}$ . . .	33
3.9	Comparison between major sandwich beam cores including re-entrant auxetic core in terms of maximum blast impulse sustained by optimal design of their respective sandwich beams . . . . .	34
4.1	A re-entrant hexagonal cell honeycomb. . . . .	35
4.2	Re-entrant hexagonal unit cell and its parameters . . . . .	36
4.3	Cell deformation by cell wall bending, giving linear-elastic extension and compression of the honeycomb due to load in $X_1$ direction . . . . .	37
4.4	Cell deformation by cell wall bending, giving linear-elastic extension and compression of the honeycomb due to load in $X_2$ direction . . . . .	38
4.5	Schematic of re-entrant hexagonal auxetic cell under shear deformation (a) Undeformed configuration (b) Deformed configuration . . . . .	39
4.6	A beam under pin-pin boundary condition and pure bending . . . . .	40
4.7	Plastic hinge formation when load is applied in $X_1$ direction . . . . .	41
4.8	The semi-infinite notch . . . . .	42
4.9	Re-entrant hexagon auxetic element node numbering . . . . .	44
4.10	Re-entrant hexagonal unit cell . . . . .	46
4.11	Configuration force in re-entrant hexagonal auxetic . . . . .	47
4.12	Free body diagram of forces in rib A-B . . . . .	47
5.1	Variation of $E_1$ vs $\theta$ for re-entrant hexagon auxetic for different $\frac{W}{l}$ . . . . .	49
5.2	Variation of $E_2$ vs. $\theta$ for re-entrant hexagon auxetic for different $\frac{W}{l}$ . . . . .	50
5.3	Variation of $\nu_{12}$ vs $\theta$ for re-entrant hexagon auxetic for different $\frac{W}{l}$ . . . . .	50
5.4	Variation of $\nu_{21}$ vs $\theta$ for re-entrant hexagon auxetic for different $\frac{W}{l}$ . . . . .	51
5.5	Variation of $G_{12}$ vs $\theta$ for re-entrant hexagon auxetic for different $\frac{W}{l}$ . . . . .	51
5.6	Loading and boundary conditions on a representative 2D rectangle ( $W = 30mm$ ) . .	52

5.7	$U_2$ displacement vectors for a model with boundary conditions given in Fig. 5.6. The red and blue arrows shows the direction of the displacement. . . . .	53
5.8	Variation of generalized elastic constants w.r.t. cell relative density of re-entrant hexagonal auxetics . . . . .	54
5.9	Comparison of theoretical plastic collapse strength and plastic collapse strength obtained by FE analysis . . . . .	55
5.10	Eigenvalue for symmetric field w.r.t. wedge angle in symmetric field . . . . .	55
5.11	Eigen values for anti-symmetric field w.r.t. wedge angle in anti-symmetric field . . . . .	56
5.12	Eigen values for re-entrant corner ( $\alpha = 75^\circ$ ) in symmetric field . . . . .	56
5.13	Re-entrant hexagon auxetic element node numbering . . . . .	57
5.14	Variation of configurational force generated w.r.t. $l$ . . . . .	58
A.1	Sandwich beam geometry . . . . .	61
A.2	Plastic hinges formation in Stage III . . . . .	64

# List of Tables

1.1	Poisson's ratio significance in isotropic solid [1] . . . . .	8
1.2	A brief summary of the historical development of auxetic materials . . . . .	8
1.3	Conventional sandwich beam core properties [8] . . . . .	15
2.1	Mesh convergence in terms of % $\delta$ error in maximum stress w.r.t 10 elements across the rib . . . . .	23
5.1	Eigen values of re-entrant hexagonal element stiffness obtained by direct stiffness method	57

# Chapter 1

## Introduction

Materials possessing negative Poisson's ratio are called auxetics materials. In this introductory chapter definition of auxetic materials and their historical development have been discussed.

### 1.1 Poisson's Ratio

Poisson's ratio is the negative ratio of transverse strain to axial strain represented as

$$\nu = -\frac{\varepsilon_{trans}}{\varepsilon_{axial}} \quad (1.1)$$

It is named after a French mathematician Siméon Poisson. The axial strain  $\varepsilon_{axial}$  is along the loading axis and  $\varepsilon_{trans}$  is the strain along the transverse direction in the above Eq. 1.1. In conventional material, when a material is subjected to uni-axial tensile stretch the axial strain  $\varepsilon_{axial}$  is positive and the transverse strain  $\varepsilon_{trans}$  is negative because of the compression experienced in lateral direction as shown in Fig. 1.1. Hence by the definition of Eq. 1.1 conventional material have positive Poisson's ratio. This phenomenon is called **Poisson effect** and Poisson's ratio  $\nu$  is the measure of this effect.

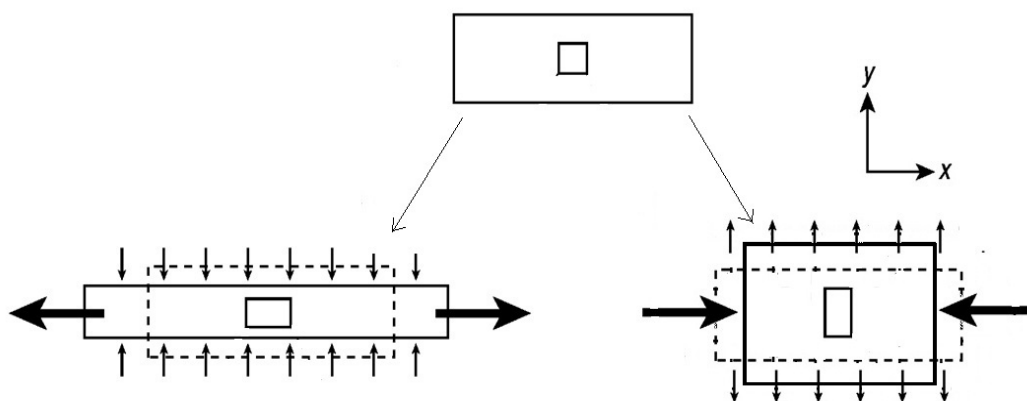


Figure 1.1: Poisson's effect on a conventional material when load is applied in x direction.

In 1807 Young [9] observed the Poisson effect during one of the lecture on "Natural Philosophy

and the Mechanical Arts". After few years, in 1827 Poisson [10] obtained a measure using a ratio called Poisson's ratio  $\nu$  defined by Eq. 1.1 and this value is 0.25 based on the molecular interaction theory. Later in 1859, Kirchhoff [11] obtained Poisson's ratio for metals using the relation between Young's modulus  $E$  and shear modulus  $G$  as defined in Eq. 1.2.

$$\frac{E}{G} = 2(1 + \nu) \quad (1.2)$$

In 1828 Cauchy's theoretical study showed that only two independent elastic moduli are necessary for characterizing the elastic behavior of isotopic materials [12], implying that Poisson's ratio of material must differ from another. Generally Poisson's ratio for different material varies from -1 to 0.5.

## 1.2 Auxetic Materials

In this section auxetic materials and few examples that exhibits negative Poisson's ratio are discussed. Followed by the five different landmark of Poisson's ratio for isotropic solids and the historical development of auxetic materials.

Auxetic materials are defined as solids that possess negative Poisson's ratio. It is derived from the Greek word *auxetikos* ( $\alpha\upsilon\chi\eta\tau\iota\kappa\omicron\varsigma$ ), which means "that which tends to increase" [13]. When auxetic materials are stretched ( $\varepsilon_{axial} < 0$ ) in one direction, they also expands in the direction transverse to the loading direction ( $\varepsilon_{trans} < 0$ ), as shown in Fig. 1.2(a). It follows that if the load is reversed from stretching to compression, the material contracts in transverse direction as depicted in Fig. 1.2(b). Few examples of 2D micro-structural geometries resulting the auxetic behavior are depicted in Fig. 1.3. In these examples some form of rotation takes place at joints for auxetic behavior to manifest. For example, in case of re-entrant hexagonal auxetic structure hinge formation at re-entrant corner gives rise to negative Poisson's ratio.

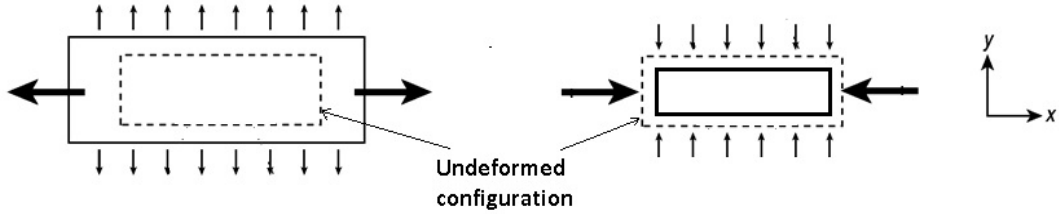


Figure 1.2: Schematic of negative Poisson's ratio effect on 2D shape

The negative Poisson's ratio materials have been studied extensively in last two decades because of their counter intuitive mechanical response. Physically negative ratio means that they expands laterally when stretched and contracts laterally when compressed [5]. Studies have shown that such type of materials exhibits enhanced mechanical properties such as higher fracture toughness [14, 15], shear modulus [16], indentation resistance [14, 17] and acoustic damping [18] compared to conventional materials. A negative Poisson's ratio for a layer permits synclastic curvature shaping [19]. Synclastic surface is curved along the same side in all direction which means center of curvature of all membrane is on the same side as shown in Fig. 1.4(b) where as, in case of anticlastic surface, any two orthogonal curvatures always has opposite signs Fig. 1.4(a). This behavior is the result of the

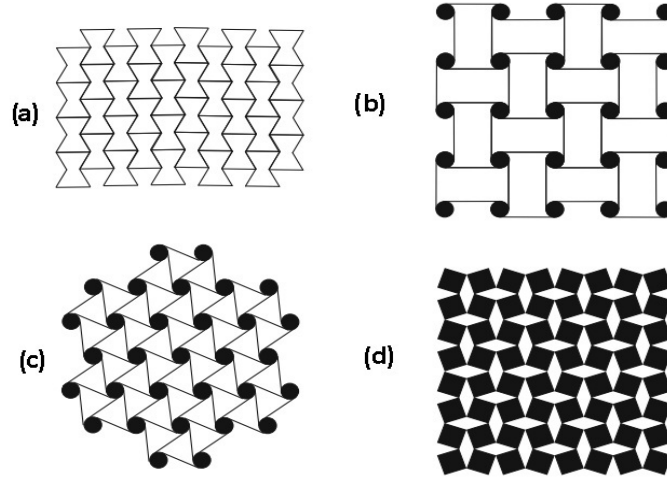


Figure 1.3: Geometries exhibiting Auxetic behavior [1]. (a) Re-entrant hexagon (b) Chiral square symmetric [2] (c) Chiral circular [2] (d) Rotating unit squares [3]

differential contraction caused by the Poisson's effect [4]. The advantage in case of sandwich panel is that synclastic curvature of auxetic core [20] allows doubly curved sandwich panel manufacturing without core buckling.

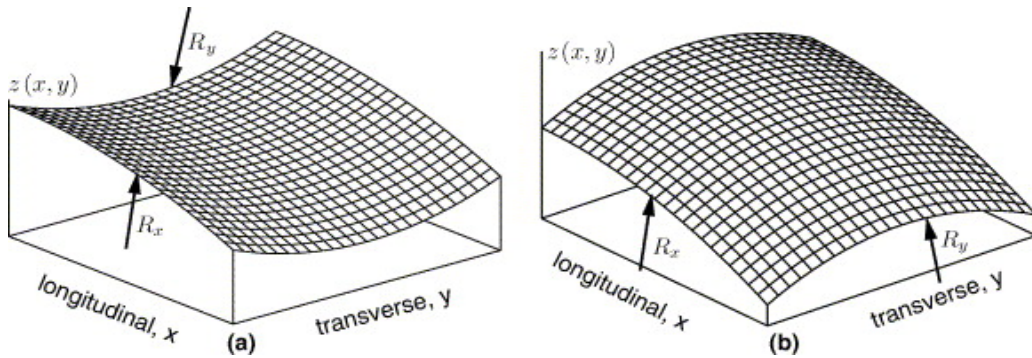


Figure 1.4: Distortion behavior of surface a) Anticlastic surface b) Synclastic surface [4].

Significance of Poisson's ratio at major landmarks [21] is summarized in Tab. 1.1. The first and well known significance is the volume preservation which is also known as condition of incompressibility, at  $\nu=0.5$ . It is also the extreme positive limit for isotropic solids. Poisson's ratio greater than 0.5 implies the negative volume which is physically not possible. Rubber has a Poisson's ratio of value close to 0.5. In case of isotropic solid possessing zero Poisson's ratio  $\nu=0$ , from the definition of Eq. 1.1 one can interpret that solid will show very little lateral deformation when compressed or stretched in axial direction, showing the preservation of cross section area. Mathematically with reference to Eq. 1.2 for isotropic solids, substitution of  $\nu=-0.5$  gives  $E = G$ . Where, the Young's modulus  $E$  and the shear modulus  $G$  are two of the most common engineering moduli used there by giving the condition of moduli preservation.  $\nu = -1$  means the same amount of positive strain in lateral direction when stretched in axial direction and vice versa when compressed in axial direction, signifying the landmark of shape preservation.

Table 1.1: Poisson's ratio significance in isotropic solid [1] .

Poisson's ratio	Physical significance
$\nu=1$	Area preservation
$\nu=0.5$	Volume preservation
$\nu=0$	Preservation of cross section
$\nu=-0.5$	Moduli reservation, $E = G$
$\nu=-1$	Shape preservation

In 1848, Saint-Venant speculated that in case of anisotropic solids, Poisson's ratio might be negative or might be greater than 0.5 [22]. Thermodynamic restrictions on isotropic elastic constitutive law gives the limit of Poisson's ratio as  $-1 \leq \nu \leq 0.5$  [23]. For detailed literature on evolution of negative Poisson's ratio one can refer to [1] which is summarized in Tab. 1.2.

Table 1.2: A brief summary of the historical development of auxetic materials

Year	Person	Discovery
1848	Adh�mar Jean Claude Barr�de Saint-Venant	Suggested $\nu < 0$
1920	Woldemar Voigt	$\nu < 0$ in single crystals
1927	Augustus Edward Hough Love	$\nu < 0$ in pyrites
1946	R.F.S. Hearmon	$\nu < 0$ in single crystals
1965	Yuan-Cheng Fung	$-1 \leq \nu \leq 0.5$ for isotropic solids
1969	Poporeka and Balagurov	$\nu < 0$ in ferromagnetic films
1970	Landau and Lifshitz	Hint on $\nu < 0$
1971	Simmons and Wang	$\nu < 0$ in single crystals
1979	Bjeletich et al.	$\nu < 0$ in composite laminates
1979	Milstein and Huang	$\nu < 0$ in FCC crystals
1980	Tsai and Hahn	$\nu < 0$ in composite laminates
1981	Kittinger et al.	$\nu < 0$ in �s-quartz
1982	Gibson et al.	$\nu < 0$ in re-entrant hexagonal honeycombs
1984	Carl T. Herakovich	$\nu < 0$ in composite laminate
1985	Robert F. Almgren	3D isotropic structures with $\nu = -1$
1987	Krzysztof Witold Wojciechowski	Hexagonal molecules ( $\nu < 0$ )
1987	Roderic S. Lakes	Foams ( $\nu < 0$ )
1987	Jaric and Mohanty versus Frenkel and Ladd	Debate on $\nu < 0$ in FCC
1988	Sun and Li	$\nu < 0$ in composite laminates
1989	Wojciechowski and Branka	Hexagonal molecules ( $\nu < 0$ )
1989	Evans and Caddock	Foams ( $\nu < 0$ )
1991	Kenneth E. Evans	Coined the term "auxetic"

Auxetic materials could be either naturally occurring or man-made. In major cases negative Poisson's ratio occurs because of their micro structure. One of the naturally occurring auxetic



material is silicon dioxide ( $\text{SiO}_2$ ) in the structure of  $\alpha$ -cristobalite structure [24]. The Poisson's ratio of  $\alpha$ -cristobalite can reach a negative maximum value of -0.5 in certain directions, where as the average Poisson's ratio for its single-phased aggregate was calculated as -0.16 by Yeganeh-Haeri et al. [24]. These are also called semi-auxetic materials [25] as only some part of it is responsible for the negative Poisson's ratio. Based on the  $\alpha$ -cristobalite Poisson's ratio due to it's structure, Keskar and Chelikowsky [26] predicted that the most common form of crystalline silica,  $\alpha$ -quartz, will also posses negative Poisson's ratio. They also investigated the elastic properties of  $\alpha$ -cristobalite and other forms of silica using first-principles computation and classical inter-atomic potential functions [26].

Poisson's ratio basically depends on the micro-structure of the material, there by auxetics can also be produced by altering the existing material micro-structures or reproducing a material with the micro-structure resulting the negative Poisson's ratio and enhanced mechanical properties. For example, Lakes [5] suggested the conversion of conventional foams to auxetic foams by permanently protruding the ribs of each cells inward, thereby resulting in a re-entrant structure. Auxetic foams can be manufactured by compressing a three dimensional foam in all three perpendicular direction and then heating it to the temperature above the softening point of the foam material as shown in Fig. 1.5. A study done by Lakes concludes that a compression factor of value 1.4-4 gives negative Poisson's ratio in case of polyester foam. Where as, reticulated metal foams need to be plastically deformed in all three orthogonal directions at room temperature without any heating [5].

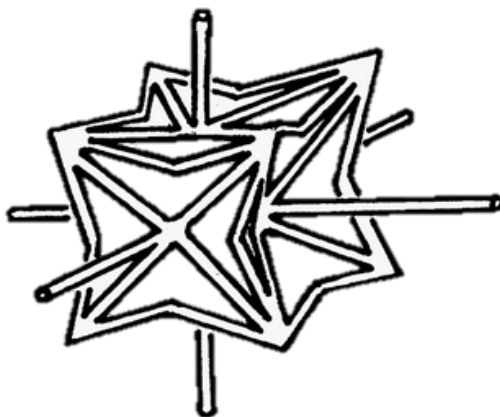


Figure 1.5: Re-entrant unit cell produced by symmetric collapse [5]

By using 3D printing technology, Critchley et al. [6] produced auxetic foam with Poisson's ratio as low as -1.18 under tensile load. A magnified image of this 3D printed auxetic microstructure is shown in Figure 1.6.

In 2005 He et. al. [27] produced a polymeric auxetic material in the form of liquid crystalline polymer (LCP). As schematic in Fig. 1.7(a) shows, initially the molecular rods are attached to the polymeric chain and oriented in the direction of molecular chain. When polymeric chain is stretched uni-axially the molecular rods re-orient them-self in the lateral direction depicting the negative Poisson effect as shown in Fig. 1.7(b). They have also synthesized a polymeric chains consisting of para-quaterphenyl rods that are transversely attached to the polymer's main chain which also results in negative Poisson's ratio.

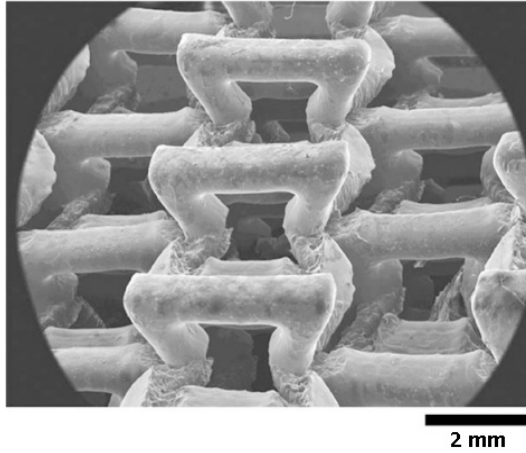


Figure 1.6: Auxetic foam by 3D printing Critchley et al. [6]

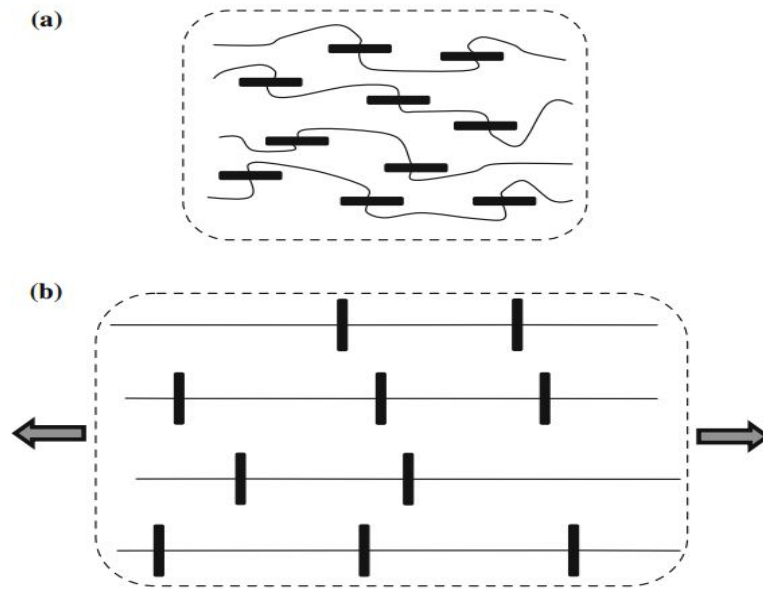


Figure 1.7: liquid crystalline polymer (LCP) (a) undeformed, and (b) deformed states [1]

### 1.3 Re-entrant Honeycomb Auxetics

In lightweight structural applications sandwich panels are one of the important composite structures being used. For the majority of applications only flat sandwich panel with honeycomb core is being fabricated. In fact studies have shown that fabrication of curved sandwich panels with conventional regular honeycomb core leads to local collapse and buckling of core. However by making suitable changes in the honeycomb geometry, curved sandwich panels can be manufactured [20]. It is possible due to negative Poisson's ratio of core allowing to form a synclastic surface as discussed in Sec. 1.2. The resulting structure from conventional regular hexagonal honeycomb having negative Poisson's ratio is called re-entrant hexagonal auxetic.

Two dimensional honeycombs with regular hexagonal cells exhibits a Poisson's ratio of  $+1$  in the honeycomb plane. Regular hexagon have angle of  $120^\circ$  between it's consecutive interior walls.

Whereas, re-entrant honeycomb is made up of hexagons that are shaped like a bow as shown in Fig. 1.8. The Poisson's ratio of re-entrant hexagonal auxetic depends upon its re-entrant angle and other geometrical parameters [28]. When the unit cell of re-entrant hexagonal auxetic is stretched in such a way that two vertices of bows are being pulled apart then whole structure expands in every direction [29]. The unit cell geometry of re-entrant honeycomb has sizeable influence on its mechanical properties [29]. Young's modulus and Poisson's ratio of these type of honeycomb can be predicted based on their deformation mechanisms [5, 30, 31, 32]. The re-entrant hexagonal auxetics have been studied thoroughly in last one decade [33, 34]. The composite material composed of regular layer of aluminum and re-entrant auxetic has a significant increase in their Young's modulus [35]. Fabrication of re-entrant foams involving compression followed by heat treatment is discussed by

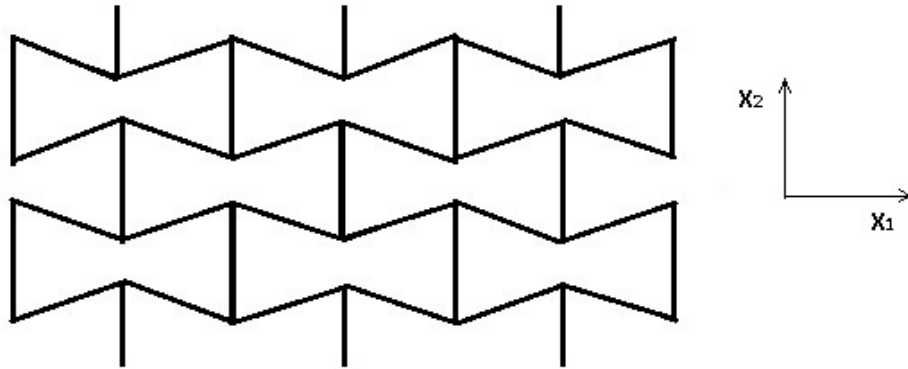


Figure 1.8: Schematic of re-entrant hexagonal auxetic

Friis et. al. [36]. In the later article authors further concludes that re-entrant transformation of metal foam involves plastic hinge formation and plastic buckling of ribs. However this fabrication methods had shortcoming including long term instability of structure and severe surface creasing [37] and those were further modified by Chan and Evans in 1997.

The unit cell of a re-entrant honeycomb is shown in Fig. 2.3 and deformation mechanism of regular hexagon honeycomb and re-entrant honeycomb can be visualized with the help of Fig. 1.9(a) and Fig. 1.9(b), respectively. It is clear from Fig. 1.9 that unlike regular hexagonal honeycomb, re-entrant hexagonal honeycomb expands laterally even when it is pulled in axial direction depicting negative Poisson's ratio from the definition in Eq. 1.1.

## 1.4 Blast and Plane Shock-wave Propagation

Blast is the detonation of an explosive material. Due to blast the energy stored in the explosives are released at a very high rate. Typically, explosive material are stored in a casing or a shell which are made from steel-walled artillery to a glass bottle. The explosive material inside the shells could be any type of high explosives such as TNT or Semtex. Blast causes damage to things in proximity through several different means, these can be enlisted as the blast wave, shock waves, fragmentation, heat and the blast wind as shown in Fig. 1.10.

Blast wave is the wave of highly compressed air generated just after the explosion which travels

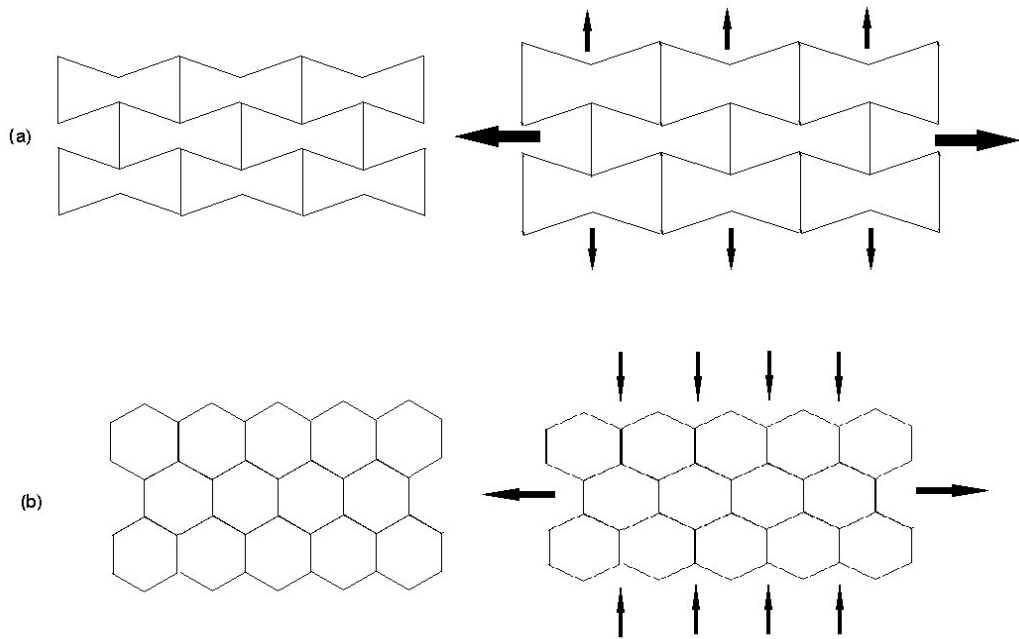


Figure 1.9: Deformation mechanism of honeycomb cores: (a) Re-entrant hexagon (b) Regular hexagon.

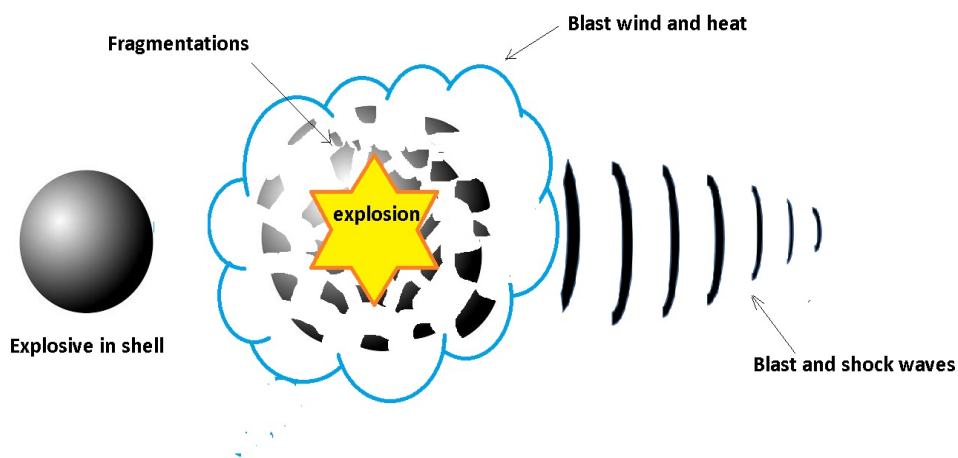


Figure 1.10: Phenomena involved in the energy release due to an explosion.

faster than the speed of sound but dissipates in matter of milliseconds over a small distance. Blast wave transfers the primary impact of the shock-waves. Shock-waves carries the energy generated in the explosion and transfers it to the structures coming on the way. For example, in case of water blast, detonation of a high explosive charge converts the solid explosive material into gaseous reaction products. The enormous pressure generated by this reaction gets transmitted to the surrounding by a spherical shock-wave travelling at a sonic speed. Detailed summary of this shock wave phenomenon

is given by Swisdak [38] and Cole [39]. Shock-waves are modelled as 2D planer waves. Shock-wave propagation is shown in Fig. 1.11 where the last wave striking the structure is assumed to be planar wave. Primary shock-wave pressure magnitude variation starting from peak pressure  $P_o$  with respect to time exponentially, is given by Eq. 1.3.

$$p(t) = p_o e^{\frac{-t}{\theta}} \quad (1.3)$$

Where,  $p_o$  is the peak pressure and  $\theta$  is the decay constant of the shock wave. The magnitude of the shock wave peak pressure  $p_o$  and decay constant  $\theta$  depend upon the mass  $m$  and type of explosive material and the distance  $r$  between the object and the location of explosion. A simple power-law scaling is supported by experimental data for these parameters in the form given below,

$$\text{Parameters} = K \left( \frac{m^{1/3}}{r} \right)^\alpha \quad (1.4)$$

Where  $m$  is the mass of explosive in kilograms and  $r$  is the distance in meters.  $K$  and  $\alpha$  are constants. For example, for an underwater TNT explosion peak pressure can be taken from Swisdak [38].

$$p_o = 52.4 \left( \frac{m^{1/3}}{r} \right)^{1.13} \quad (\text{in MPa}) \quad (1.5)$$

where as the decay constant is given by

$$\theta = 0.084 m^{1/3} \left( \frac{m^{1/3}}{r} \right)^{-0.23} \quad (\text{in ms}) \quad (1.6)$$

Similarly, pressure wave parameters for few more materials can be directly taken from Table 2 of Swisdak [38].

In case of blast wave in air, a primary shock wave generated due to detonation of explosive travels at near sonic speed with an exponential pressure-time history at any fixed location from the explosive. The time constant  $\theta$  for the pulse is similar in magnitude to that of in water, but the peak pressure is of lower magnitude [40].

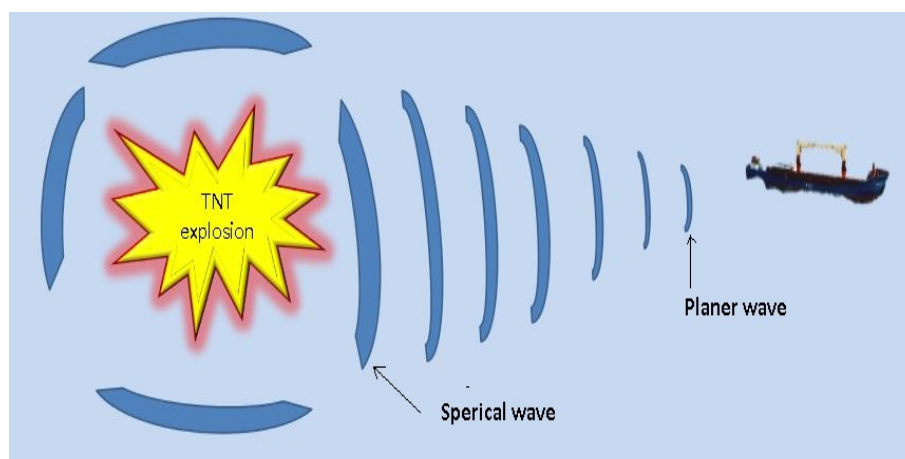


Figure 1.11: Shockwave propagation in water

## 1.5 Sandwich Beams

Sandwich beams are widely used in light structured applications. They are preferred over monolithic beams because of their higher strength to weight ratio. Strategically important vehicles need to be lighter and faster which automatically turns the preference towards sandwich beams. Sandwich beams are comprised of mainly three parts, namely front face sheet, core material and rear face sheet as shown in Fig. 1.12.

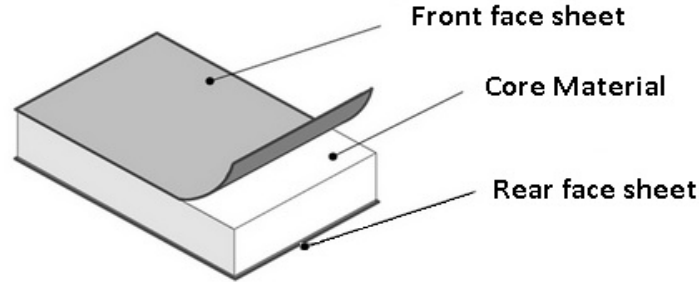


Figure 1.12: Sandwich beam

Among these major parts mainly core material governs the mechanical behavior of sandwich beams. In recent years a number of micro-architected materials have been developed to use as the cores of sandwich beams and panels including pyramidal cores, diamond-celled lattice materials, metal foams, hexagonal-honeycombs and square-honeycombs cores. Geometry of some of them is shown in Fig. 1.13. Core materials are periodic cellular materials having 20% or less of their volume occupied by parent material [40].

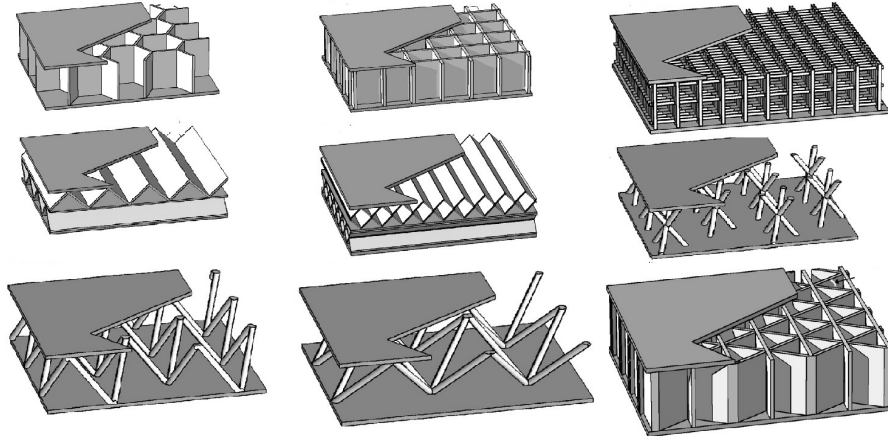


Figure 1.13: Sandwich beam core topologies [1].

Fleck and Deshpande [8], in 2004 proposed an analytical method based on momentum transfer model to study the blast resistance of sandwich beams. This analytical model requires the normal compressive strength  $\sigma_{ny}$  and longitudinal strength  $\sigma_{ly}$  to obtain the blast resistance of the sandwich structures. The normal compressive strength and longitudinal strength for various conventional core topologies are given in the Tab. 1.3.

However, there are only limited studies were done till date on the compressive strength of the

Table 1.3: Conventional sandwich beam core properties [8]

Core Design	$\sigma_{ny}/\sigma_y$	$\sigma_{ly}/\sigma_y$
Pyramidal core	$0.5\bar{\rho}$	0
Metal foam core	$0.3\bar{\rho}^{3/2}$	$0.3\bar{\rho}^{3/2}$
Hexagonal honeycomb core	$\bar{\rho}$	0
Square honeycomb core	$\bar{\rho}$	$0.5\bar{\rho}$
Diamond-celled core	$0.5\bar{\rho}$	$\bar{\rho}$
Ideal core	$\bar{\rho}$	$\bar{\rho}$

auxetic cores. Miller et. al. [41] estimated the normal compressive strength of the re-entrant auxetic core experimentally. They have observed 13% increase in normal peak stress then the regular hexagonal honeycomb, that is  $\sigma_{ny}/\sigma_y$  and  $\bar{\rho}$  is related as follows:

$$\frac{\sigma_{ny}}{\sigma_y} = 1.13\bar{\rho} \quad (1.7)$$

And in order to characterize the blast resistance of auxetic core based on Fleck and Deshpande [8] approach one also needs an estimate of the longitudinal compressive strength of the auxetic cores. However, no such studies were conducted to the authors knowledge. This motivated us to perform the Monte Carlo simulations to obtain the longitudinal strength of the composites, the detailed overview is presented in the Sec. 2.1.

## 1.6 Blast resistance of Sandwich beams

As discussed earlier, sandwich beams play a crucial role in mitigating the impact or blast loading, for example in defense sectors of Naval and Aerospace industries. In these industrial sectors, structures with high strength/weight and stiffness/weight ratios plays a vital role due to their demand for light weight structures. Sandwich beams are composite structures consists of a metallic core sandwiched between a face and rear sheets as shown in Fig. 1.12. And hence sandwich cores are lighter and meets the demands in the reducing the weight of those structures. Further, Sandwich beam properties assists in dispersing the mechanical impulse transmitted into structure and thus protecting components present behind it.

The behavior of sandwich panels under blast loading have been widely studied in the last two decades. Fleck and Deshpande [8] have theoretically studied the dynamic response of sandwich beams under air and underwater blast loading using three stage momentum transfer based model. They divided the structural response into three sequential steps and then developed performance charts of the sandwich beams with different core materials in order to find an optimal design.

Experimental studies were performed by several authors [42, 43, 44] on the blast resistance of sandwich structures. Most of these studies are pertaining to metallic honeycomb core. These studies observed that by altering the topological parameters of the core to optimum values, the damage of rear sheet can be reduced. Radford et. al. through their metal foam impact loading experiments [45] concluded that sandwich panels has ability to resist dynamic loading far more than that of monolithic metal plates having same areal density. Following to previous work, the behaviors of designable micro structure core materials have been studied [46, 47] under blast loading. Xu and Hutchinson

[48] conducted three dimensional finite element simulations for the structural response of sandwich beams with various cores e.g. squared honeycomb core, pyramidal core and corrugated cores. This analysis give coherent results with the Fleck and Deshpande's estimations [8].



## Chapter 2

# Blast Resistance of Sandwich Beam Comprising Auxetic Core

In this chapter we are discussing the methodology to obtain the longitudinal compressive strength of re-entrant hexagonal auxetic. Later we are implementing the three stage momentum transfer model to construct the performance chart of blast resistance of sandwich beam comprising re-entrant hexagonal auxetic core and compare its blast mitigation with the other conventional cores.

### 2.1 Motivation of Study

Blast resistance of sandwich beams have been extensively studied for conventional core topologies as discussed in Sec. 1.6. However, the blast resistance of sandwich structures with auxetic cores are not fully understood so far. In a sandwich beam the function of conventional core is to disperse the impulse and dissipate the energy transferred to the beam. In case of auxetic cores, they come with additional confinement due to their nature of exhibiting negative Poisson's ratio. Through this study we try to understand the auxetic core influence on mitigating the blast or impact loading of the sandwich beam structures.

The core idea in a sandwich structure is the unity in strength through composites. However in case of auxetics, confinement effects are observed due to their negative Poisson's ratio. The manifestation of lateral confinement is observed in the indentation test. In case of non-auxetic material when an indentation is made, material flows outwards from the point of indentation. But in case of auxetics the material flows towards the point of indentation as a consequence of negative Poisson's ratio they possess as shown in Fig. 2.1. Out of all possible auxetics, we are selecting a re-entrant hexagonal structure because it exhibits meta-material properties as discussed in the Sec. 1.2. These are cellular solids where a representative unit cell homogenization can be used to get the mechanical properties. We want to study the blast mitigation of sandwich structure with auxetic core and compare with the other conventional cores. we are using the three stage momentum transfer model as it allows us to construct performance charts which industries can directly use as per the requirements.

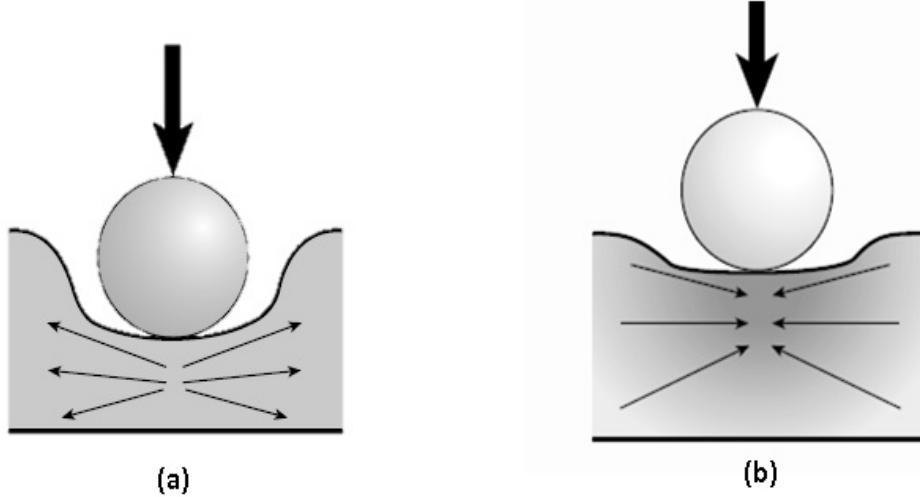


Figure 2.1: Material flow direction on indentation (a) Non-auxetics material (b) Auxetic materials [7].

## 2.2 Introduction

As discussed in Sec. 1.5, sandwich panels are widely used in lightweight structural applications. Under these applications their properties i.e. high strength to weight ratio and high stiffness to weight ratio plays an important role [49]. Strategically important vehicles are prone to face impact loading due to blasts occurring in near proximity. There by, Sandwich structures with high blast resistance have important role in designing strategically important vehicles. Resistance against blast of a sandwich panel is governed by the type of core material present in it. Recently a wide number of micro-architected sandwich core materials have been developed including hexagonal honeycomb core [50], pyramidal truss core, tetrahedral truss core [51], Corrugated and diamond ducts [52] etc. shown in Fig. 1.13.

An analytical model, established [8] by Fleck and Deshpande, is used to estimate the structural response of sandwich beams based on the core materials properties using momentum transfer based approach. There dynamic structural response of sandwich beams have been theoretically studied under air and underwater blast.

The present study aims to implements three stage momentum transfer model on a sandwich beams comprised of re-entrant honeycomb auxetic core material. Auxetics as explained in Sec. 1.2, also known as mechanical meta-material, are those material possessing negative Poisson's ratio [53]. Poisson's ratio  $\nu$  is defined in tension as the negative ratio strain in the transverse direction to the strain in the longitudinal direction. Physically negative ratio means they expands laterally when stretched and contracts laterally when compressed [5]. Studies have shown that such type of materials exhibits enhanced mechanical properties such as higher fracture toughness [14, 15] and shear modulus [16], indentation resistance [14, 17] and also acoustic damping [18] compared to conventional materials. The advantage in case of sandwich panel is that negative Poisson's ratio allows synclastic curvature of plates [20] due to which doubly curved sandwich panels can be easily manufactured without core buckling.

Auxeticity of a micro-structure is due to its structural configurations [54]. The common auxetic

materials includes chiral rotating triangles, chiral rotating circles, chiral rotating rectangles, re-entrant honeycomb [55], Hexachiral lattice etc. We are limiting ourselves to re-entrant hexagonal type auxetic core in this study. The mechanical behavior of auxetic core such as normal compressive strength  $\sigma_{ny}$  and the longitudinal strength  $\sigma_{ly}$  are required for the above mentioned three stage modelling of sandwich beams [8]. Obtaining relation of normal compressive strength  $\sigma_{ny}$  and longitudinal strength  $\sigma_{ly}$  with the uni-axial yield strength  $\sigma_y$  of parent material experimentally for auxetic core is highly cumbersome. Hence the objective of our study is to investigate the mechanical behavior of auxetic material for various geometric configuration using finite element simulations. We obtained the mechanical properties by modelling each cell as representative unit volume and estimated the longitudinal compressive strength using spatially homogenized equivalent stress approach. Monte Carlo based finite element simulations for various geometric configurations are carried out in commercial finite element package ABAQUS and relation between the density and the mechanical behavior of auxetic core is obtained. Using three stage momentum transfer model, the non-dimensional transverse displacement  $\bar{w}$  and longitudinal tensile strain  $\epsilon_c$  accumulated in an auxetic sandwich beam is calculated as a function of blast loading magnitude and the performance charts are obtained.

## 2.3 Methodology

In this section we have introduced the methodology to estimate the longitudinal compressive strength using the finite element analysis and representative unit cell homogenization. Later we have implemented the three stage momentum transfer model [8] to blast resistance of sandwich beam and constructed the design charts.

### 2.3.1 Representative Unit Cell Homogenization

Obtaining the generalized mechanical properties such as the longitudinal strength and normal compressive strength of the auxetic core is very cumbersome because of the complex shape of re-entrant hexagon as well as in order to find a generalized properties one has to perform several experiments. To overcome this difficulty we have done Monte Carlo's study over a wide range of topological parameter of re-entrant hexagonal structure and with non-intersection constraint on point A and point B (See Fig. 2.2) as given in Eq. 2.3.1. Auxetic core has a repetitive cell. And, we want to represent the behavior of each individual cells. In order to do that we are using first order theories by homogenization. Representative unit cell is the cell that effectively includes all the sampling of all micro-structural heterogeneities that exist in overall structure.

Macroscopic equivalent stress obtained by the spatial averaging can be taken as follows.

$$\sigma_{eq} = \frac{1}{V} \int_V \sigma dV \quad (2.1)$$

Here we have selected elements critical location for homogenization shown in Fig. 2.3. A spatially weighted averaging technique have been employed over the representative unit cell in order to achieve homogenization. Weights of the element is assigned according to its location in the unit cell. For the cell under study weight of the elements are as given below

$$W_1 = W_3 = W_4 = W_6 = \frac{W + H/\sin\theta}{4(W + 2H/\sin\theta)} \quad (2.2)$$

$$\bar{w} > 2 \cot \theta$$

$$W_2 = W_5 = \frac{H/(\sin\theta + \tan\theta)}{2(W + 2H/\sin\theta)} \quad (2.3)$$

Where  $W_1$ ,  $W_2$ ,  $W_3$ ,  $W_4$ ,  $W_5$  and  $W_6$  are weights assigned to element 1,2,3,4,5 and 6 respectively (see Fig. 2.3). Also  $W$ ,  $H$ ,  $t$  and  $\theta$  are the geometric parameters as shown in Fig. 2.2.

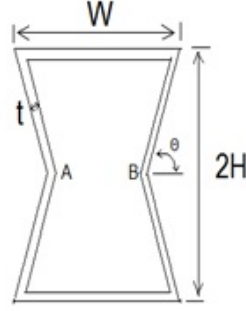


Figure 2.2: Geometric parameters of representative unit cell

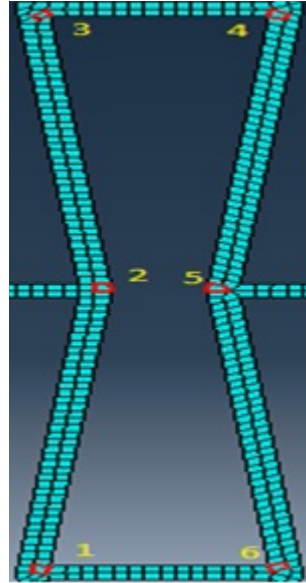


Figure 2.3: Representative unit cell of re-entrant honeycombs. Elements with red boundary have been chosen for homogenization.

Re-entrant honeycomb is a cellular solid and most important characteristic of a cellular solid is its relative density,  $\rho^*/\rho_s$  ( $\rho^*$ , the density of cellular solid divided by parent material density,  $\rho_s$ ), also can be called the packing fraction of the cellular solid [32]. The packing fraction factor of the representative unit cell of re-entrant honeycomb can be expressed by

$$PF = \bar{\rho} = \frac{2\bar{t}}{\bar{w}\sin(\theta)} + \frac{\bar{t}}{2} \left( \frac{2}{\bar{w}\tan\theta} - \frac{\bar{t}}{2\bar{w}\tan\theta} \right) + \frac{\bar{t}}{2} \left( 2 - \frac{2\bar{t}}{\bar{w}\sin\theta} - \frac{\bar{t}}{\bar{w}\tan\theta} \right) \quad (2.4)$$

Where,  $\bar{w}, \bar{t}$  are non-dimensional geometric parameters defined as

$$\bar{w} = \frac{W}{H}, \bar{t} = \frac{t}{H} \quad (2.5)$$

$$\sigma_{eq} = \sum_{i=1}^n W_i \sigma_i \quad (2.6)$$

Re-entrant hexagonal structure has many parameters to uniquely define its geometry. Depending upon the various topological parameters the same relative density can be obtained by different combination of parameters.

### 2.3.2 Finite Element Modelling

We have done a static compressive analysis of re-entrant honeycomb auxetic structure in commercial finite element package ABAQUS. In order to find homogenized equivalent properties of re-entrant hexagon auxetic core we have used weighted averaging technique on a representative unit cell as explained in the Sec. 2.3. The parent material of the auxetic structure under study is Aluminum having the following properties

$$E = 73.7GPa, \nu = 0.33, \sigma_y = 439.6MPa$$

Based on the stress pattern over the representative unit cell, elements at critical location have been selected for the stress homogenization as shown in Fig. 2.3. Monte Carlo simulation over 480 sets of geometrical parameters have been run to establish an essential relation in the given form to implement the analytical model of dynamic response.

$$\sigma_{ny} = C \bar{\rho}^n \sigma_y \quad (2.7)$$

$C$  and  $n$  is the unknowns to be find. Packing factor  $\bar{\rho}$  is the function of geometric parameters  $W, H, t$  and  $\theta$  as explained in Sec. 2.3.

The element we have used in here is the three dimensional 8 noded hexahedral element namely, C38DR. Mesh size was determined using mesh convergence analysis (Sec. 2.3.3).

### 2.3.3 Mesh convergence study

In finite element analysis the most overlooked issue that affect the accuracy is mesh convergence. It refers to the estimation of element size to be used in the analysis to ensure that the results of an analysis are not affected by further changing the size of the mesh. The degree of requirement of mesh convergence study depends upon the geometry of model to be analyzed, especially when there is notch or irregularity present.

The formal method of establishing mesh convergence requires a curve of a critical result parameter at a specific location, to be plotted against any measure of mesh density. Minimum three convergence runs are be required to plot a curve which can be used to indicate when convergence is achieved or,

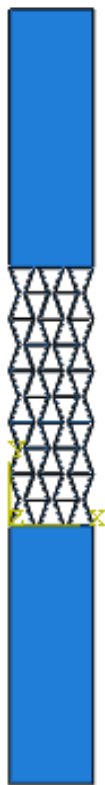


Figure 2.4: Re-entrant hexagon model



Figure 2.5: Loading and Boundary conditions

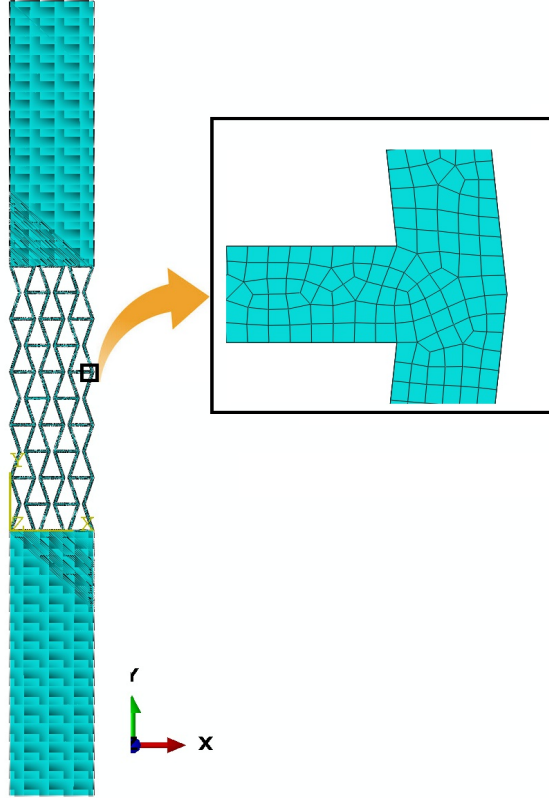


Figure 2.6: Re-entrant model mesh with 6 element across the cell rib thickness and zoomed view

how far away the most refined mesh is from full convergence. Typically the result parameter used in the convergence curve is stress instead of displacement as displacement converges faster than stress.

Here, in this study mesh convergence curve, in Fig. 2.7, includes maximum average stress with respect to number of element in the thickness direction. The relative percentage error with respect to 10 elements across the rib varies as given in the Tab. 2.1.

Table 2.1: Mesh convergence in terms of %  $\delta$  error in maximum stress w.r.t 10 elements across the rib

No. of element	% $\delta$ error	Total no. of elements
2	54.95	213691
4	37.23	441306
5	13.82	683886
6	8.94	988119
7	5.69	1344123
8	4.07	1753509
10	0	2745036

So from mesh convergence study we concluded that 6 element ( $\delta$  error < 10%) across the rib thickness would be reasonable to perform the analysis keeping in mind the computational cost would increase drastically (i.e. the total number of element will increase as given in Tab. 2.1)if we refine mesh further.

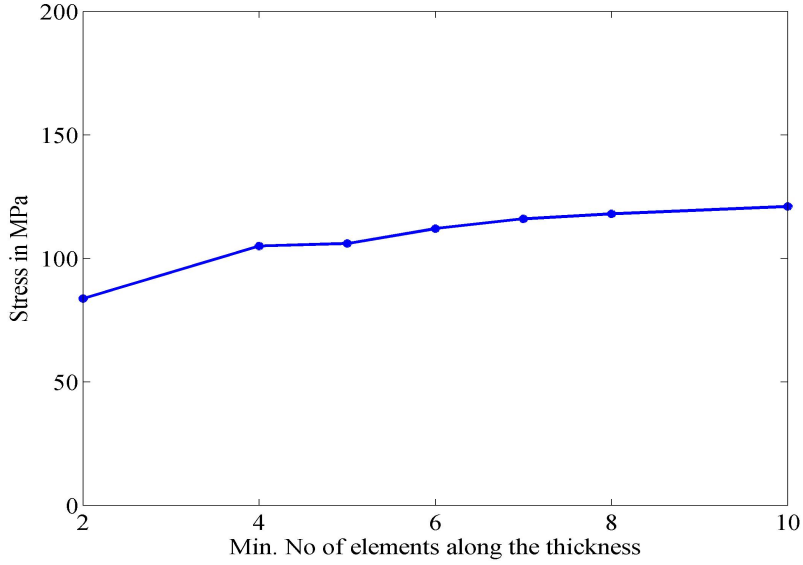


Figure 2.7: Mesh convergence curve for re-entrant hexagon model

### 2.3.4 Three Stage Momentum Transfer model

Fleck and Deshpande [8] has proposed the three stage momentum transfer model for estimating the blast mitigation of sandwich beams underwater blasting. In their analysis they considered shockwave as a planar wave and obtained magnitude of blast impulse generated due to underwater explosions is using the power law (Eq. 1.4) as mentioned in the Sec. 1.4.

In their analysis, the structural response of sandwich beams subjected to blast loading have been divided into three subsequent stages. The significance of the three stage division is based on the observance in three different time periods of these individual stages. The detailed analysis of this theory can be founds in Fleck and Deshpande [8]and here we are discussing briefly for brevity. The key mechanisms involved in these three stages is as follows.

Stage I comprises the acceleration of front face sheet to a velocity  $v_o$  by fluid-structure interaction problem as a function of impulse transferred by primary shockwave. Stage II is the phase of core crush, where momentum transfer equalizes the velocities of front face sheet and core. The loss in energy is assumed to be dissipated by plastic dissipation in compressing the core. The Stage III have been divided into two phases comprising the dissipation of the kinetic energy acquired from stage I and stage II. The phase 1 includes the formation of plastic hinges as the beam yields and continues until the travelling hinges coalesce at the mid-span. In phases 2 they determine the maximum deflection of vibrating rear face sheet [8].

#### **Stage I : Fluid structure interaction:**

Shock wave have been idealized as a planar wave falling normally and uniformly over the top face sheet. Variation of overall pressure magnitude could be mainly because of incoming pressure wave, reflection wave and rare-faction wave magnitudes. The net pressure on the front face sheet can be



given by

$$P(x, t) = P_I + P_{r1} + P_{r2} = P_o [e^{-(t+x/c_w)/\theta} + e^{-(t-x/c_w)/\theta}] + \rho_w c_w \dot{w} \left( t + \frac{x}{c_w} \right) \quad (2.8)$$

Where  $P_I$ ,  $P_{r1}$ ,  $P_{r2}$  are incoming pressure wave, reflection wave and rarefaction wave magnitudes respectively. Here a typical assumption of a blast wave of exponential shape have been made having  $P_o$  as the peak pressure and  $\theta$  as the time decay constant. The origin is taken at the front face sheet of the sandwich panel. After applying the boundary conditions on the governing equation of motion of face sheet, deflection with respect to time is given by

$$w(t) = \frac{2p_o\theta^2}{m_f(\psi - 1)\psi} [(\psi - 1) + e^{-\psi t/\theta} - \psi e^{-t/\theta}] \quad (2.9)$$

where  $\psi = \rho_w c_w \theta / m_f$ .

Till the instant liquid gets cavitated and the front sheet ceases, the impulse transferred is given by

$$I_{trans} = \xi I \quad (2.10)$$

Where,  $\xi = \psi^{\frac{-\psi}{\psi-1}}$

Velocity  $v_o$  at the end of stage I is found out using momentum balance in front face sheet.

$$v_o = \frac{I_{trans}}{m_f} \quad (2.11)$$

Where,  $m_f$  is the mass of face sheet.

### Stage II : Phase of core compression:

In this stage the core gets compressed by the advancement of the front face sheet. The velocity gained by the impulse transferred decreases because of deceleration by the core while the core and the rare face sheet accelerates. Fleck and Deshpande [8] have considered a one dimensional model by slicing through the thickness. The core is treated as rigid and ideally plastic crushable solid having nominal compressive strength  $\sigma_{ny}$  up to a nominal densification strength  $\epsilon_D$ . After reaching the densification limit  $\epsilon_D$  the core is assumed to be rigid.

By momentum conservation gives the common velocity  $v_f$  of face sheet and core during the core crushing phase as

$$(2m_f + \rho_c c) v_f = m_f v_o \quad (2.12)$$

Where  $v_o$  is the initial velocity gained by the impulse transferred from stage I,  $\rho_c$  is the core density. The energy loss  $U_{lost}$  during the core crushing is dissipated by plastic dissipation in core.

$$U_{lost} = \sigma_{ny} \epsilon_c c \quad (2.13)$$

where,  $\epsilon_c$  is the average compressive strain in the core.

### Stage III : Dynamic structural response of sandwich beam

This stage includes plastic bending and stretching because of which the kinetic energy acquired by beam in stage I and II gets dissipated. The problem under consideration is similar to the classic problem where dynamic response of a clamped beam has to be found out [8]. Jones and Symmonds [56] have developed analytical methods for large and small displacements respectively using energy

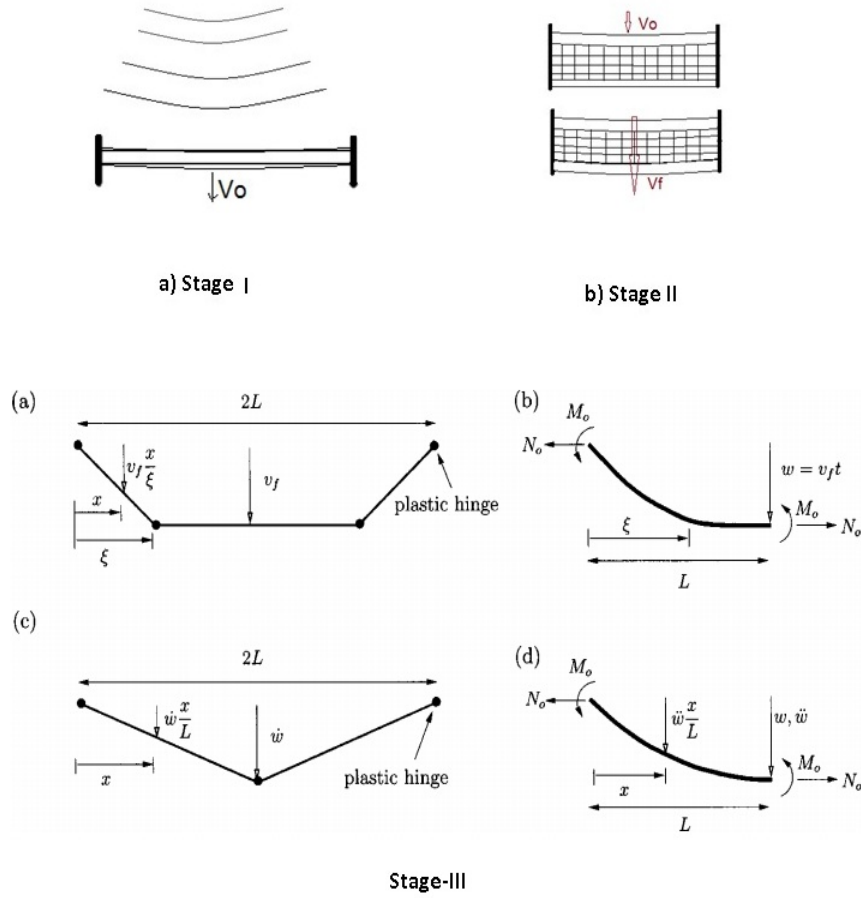


Figure 2.8: Three stages of dynamic response of sandwich beam to impulse (a) Stage-I b) Stage-II (c) Stage-III

method. The motion of the beam is separated into two phases as per the small displacement analysis of Symmonds [57]. In Phase I plastic hinges forms at the clamped ends and travels towards the center of beam as shown in Fig. 2.8(c). Angular momentum conservation is used in Phase I in order to find displacement of the mid span at the instant when hinges travelling from both the ends coalesce at the mid span as the face sheet gets stretched and rotated about the hinge. At the end of phase I the rare face sheet get completely yielded and can be assumed as string. The equation of motion depicts the harmonic motion of the beam. Using this equation of motion one can find the maximum displacement of the rare face sheet which is the ultimate aim of this analytical model [8]. The non-dimensional parameters is used in constructing the generalized design charts. Non-dimensional geometric parameters are

$$\bar{c} \equiv \frac{c}{L}, \quad \bar{h} \equiv \frac{h}{L} \quad (2.14)$$

and non-dimensional relative density is

$$\bar{\rho} \equiv \frac{\rho_c}{\rho_f} \quad (2.15)$$

The non-dimensional time response ( $\bar{T}$ ) and impulse ( $\bar{I}$ ) are given by

$$\bar{T} \equiv \frac{T}{L} \sqrt{\frac{\sigma_{fy}}{\rho_f}}, \quad \bar{I} \equiv \frac{I}{L \sqrt{\rho_f \sigma_{fy}}} \quad (2.16)$$

Where  $c, h$  and  $L$  are topological parameters as shown Fig. 2.9. The detailed formulations by the Fleck and Deshpande can be found in the Appendix A.

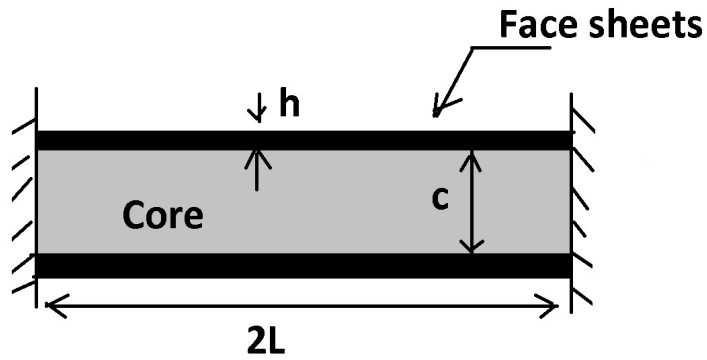


Figure 2.9: Sandwich beam geometry

## Chapter 3

# Results and Discussions: Blast Resistance of Sandwich Beams Comprising Auxetic Core

In this chapter mechanical properties of re-entrant hexagonal auxetic structure obtained by Monte-Carlo simulations is discussed. Design charts have been generated by implementing the three stage momentum transfer for re-entrant hexagonal auxetics.

### 3.1 Mechanical Properties of Re-entrant Honeycomb

The parametric study over the geometric parameter range gives the mechanical properties of the re-entrant honeycomb auxetic lattice structure. We get the  $\sigma_{eq}$  and  $\sigma_{app}$  output from the finite element simulation carried in ABAQUS. The  $\sigma_{eq}$  at  $\sigma_y$  is assumed to be  $\sigma_{ly}$ . The schematic of plot between  $\ln(\frac{\sigma_{ly}}{\sigma_y})$  vs  $\ln \bar{\rho}$  is shown in Fig. 3.1.

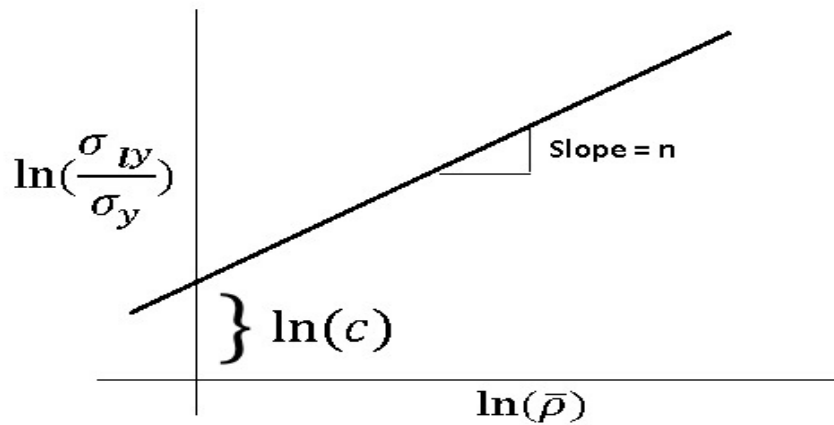


Figure 3.1: Schematic : Plot between  $\ln(\frac{\sigma_{ly}}{\sigma_y})$  vs  $\ln \bar{\rho}$

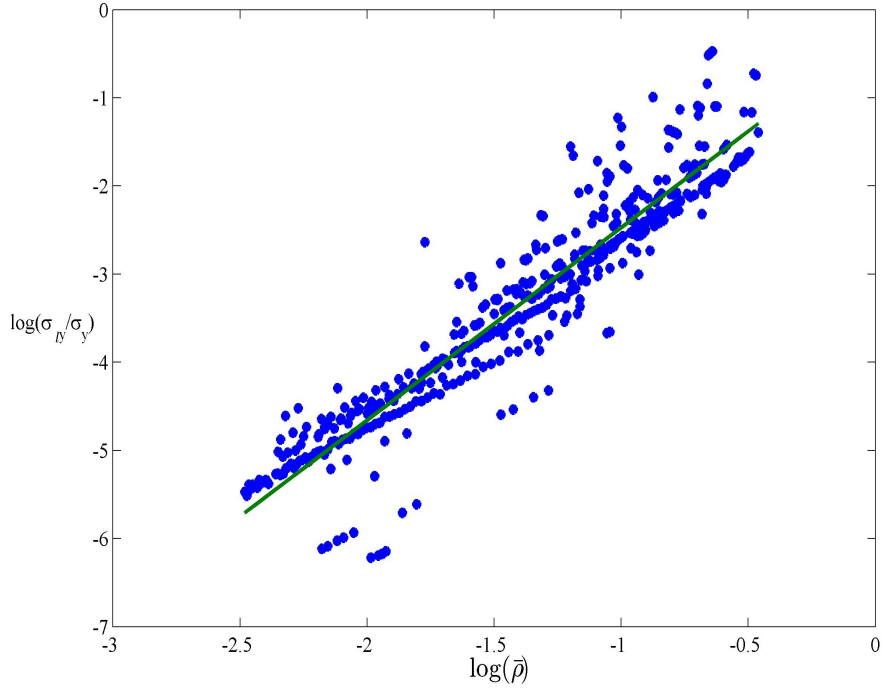


Figure 3.2: Data points obtained from the Monte Carlo analysis using finite element simulations of auxetic lattice structure.

$$\frac{\sigma_{ly}}{\sigma_y} = C\bar{\rho}^n \quad (3.1)$$

$$\ln\left(\frac{\sigma_{ly}}{\sigma_y}\right) = \ln C + n \ln \bar{\rho} \quad (3.2)$$

Plot between  $\ln\left(\frac{\sigma_{ly}}{\sigma_y}\right)$  vs  $\ln \bar{\rho}$  is shown in Fig. 3.2.

The constants obtained from the Fig. 3.2 makes the Eq. 3.1 as

$$\frac{\sigma_{ly}}{\sigma_y} = 0.75\bar{\rho}^{2.18}, \quad (3.3)$$

for an re-entrant hexagonal auxetic lattice structure.

## 3.2 Performance Charts for Under Water Blast Resistance

In this section performance charts for re-entrant hexagonal honeycomb for an underwater blast have been constructed. Different parameters for design have been taken into the consideration in order to provide design charts for all cases.

The relationship developed in Sec. 3.1 for re-entrant honeycomb structure longitudinal compressive strength  $\sigma_{ly}$  is used in constructing the performance charts for a sandwich beam using the three stage momentum transfer based analytical model [8]. Whereas the normal compressive strength  $\sigma_{ny}$  is used from the study of Miller et. al. [41]. The three stage momentum transfer model based analysis

gives the deflection  $\bar{w}$ , response time  $\bar{T}$ , the core compression  $\epsilon_c$  and the maximum tensile strain  $\epsilon_m$  in the sandwich beam in terms of loading parameters (i.e. Blast impulse  $\bar{I}$  and fluid structure interaction parameter  $\bar{\psi}$ ), beam geometry ( $\bar{c}$  and  $\bar{h}$ ), and core properties ( $\bar{\rho}$ ,  $\sigma_{ny}$ ,  $\sigma_{ly}$ ,  $\epsilon_D$ ).

We begin with the analyzing the functional dependence of deflection  $\bar{w}$  and response time  $\bar{T}$  on non-dimensional blast impulse  $\bar{I}$ .

A sandwich beam representing parameters  $\bar{c}=0.1$ ,  $\bar{h}=0.1$  with re-entrant hexagon core  $\bar{\rho}=0.1$  made of same material as that of face sheet with tensile ductility  $\epsilon_Y=0.2\%$  is considered. Using the fluid structure interaction parameter  $\psi=1.78$  which is representative of water blast with time constant  $\theta = 0.1ms$  for a 10mm thick face sheet [8] functional dependence of ( $\bar{w}$  &  $\bar{T}$ ) and ( $\epsilon_c$  &  $\epsilon_m$ ) is being plotted in Fig. 3.3 and Fig. 3.4, respectively. Core densification strain for the core is  $\epsilon_D=0.5$ .

In Fig. 3.4, the compressive strain  $\epsilon_c$  in stage II is less than densification  $\epsilon_D$  for  $\bar{I}<0.049$  and correspondingly in Fig. 3.3, normalized deflection of inner face  $\bar{w}$  varies non-linearly with respect to  $\bar{I}$ . Also, Fig. 3.3 shows that the time response for auxetic cored sandwich beam is independent of impulse at higher impulse. The reason for it can be observed in Fig. 3.4 where the core compression reaches the densification limit and then after the core compression is fixed which means that beam behaves as stretched plastic string at higher impulse. As a result,  $\bar{w}$  also varies linearly after densification limit has been reached, i.e.  $\bar{I}>0.049$ .

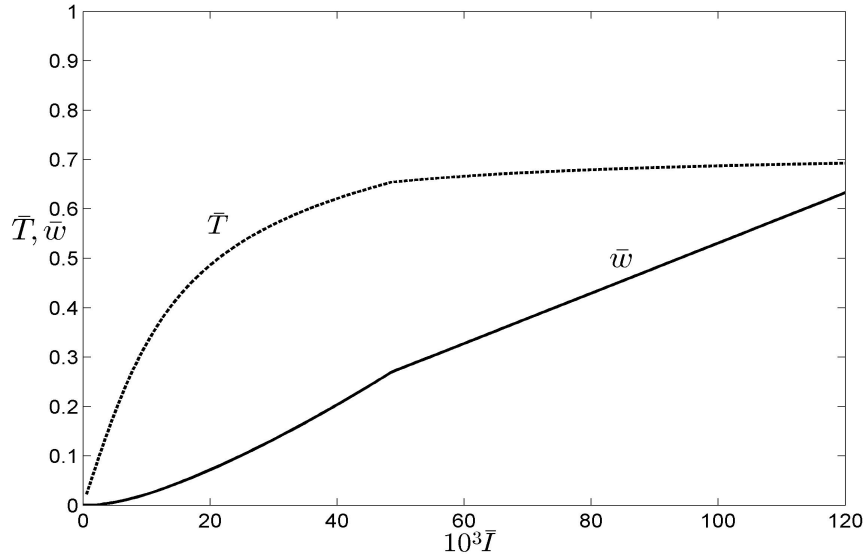


Figure 3.3: Normalized time response  $\bar{T}$  and normalized deflection  $\bar{w}$  of inner face of sandwich beam ( $\bar{c}=0.1$ ,  $\bar{h}=0.1$ ) with auxetic core ( $\bar{\rho}=0.1$ ,  $\epsilon=0.002$ ,  $\epsilon_D=0.5$ ) w.r.t. to normalized impulse  $\bar{I}$  for

For simplicity we have assumed the core material same as that of face sheet. Figure 3.5 includes the design chart for a sandwich beam with axes as design parameters  $\bar{c}$  and  $\bar{h}$  comprising auxetic core ( $\bar{\rho}=0.1$ ,  $\epsilon=0.002$ ) under a non-dimensional impulse  $\bar{I} = 2 \times 10^{-3}$ . The face sheet and core is made of steel and the densification strain  $\epsilon_D$  of the core is taken 0.5 and the tensile ductility is taken as  $\epsilon_Y=0.2$ . From the design chart, contours of  $\bar{w}$  and  $\epsilon_c$  shows that both  $\bar{w}$  and  $\epsilon_c$  increase with decreasing  $\bar{c}$ .

The top left region in Fig. 3.5 is tensile tearing failure region of the sandwich beam with auxetic

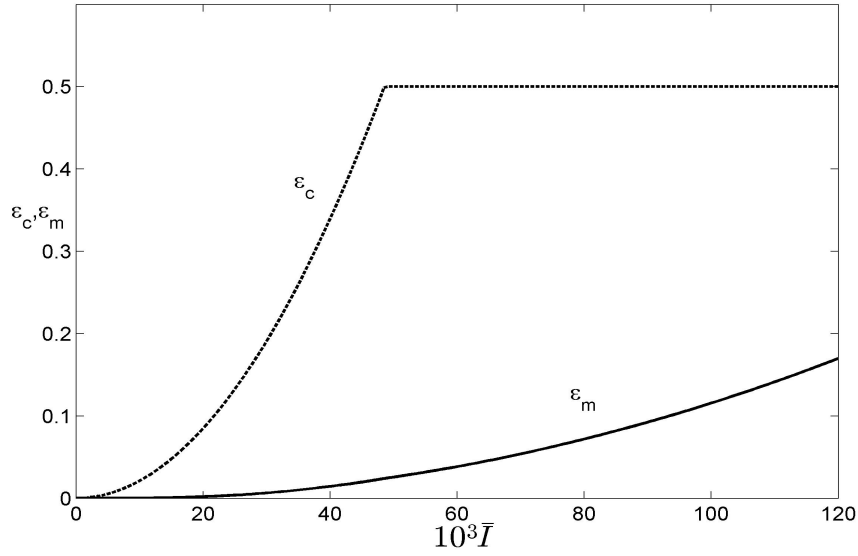


Figure 3.4: Tensile strain  $\epsilon_m$  and tensile strain of beam ( $\bar{c}=0.1$ ,  $\bar{h}=0.1$ ) with auxetic core ( $\bar{\rho}=0.1$ ,  $\epsilon=0.002$ ,  $\epsilon_D=0.5$ ) w.r.t. to normalized impulse  $\bar{I}$

core. The dependence of fluid structure interaction parameter  $\bar{\psi}$  on this region is shown in Fig. 3.6 with all other parameters taken same as previous. The tensile failure region shift to left with the decreasing value of  $\bar{\psi}$ . It is concluded that with the decreasing value of  $\bar{\psi}$  tensile failure region is less likely to occur. Comparison between the regular hexagon core and re-entrant hexagonal core is made in Fig. 3.7 in term of the chances of tensile failure to occur. The behavior of tensile failure region is same as that of auxetic core but there is always an offset between auxetic core and hexagonal honeycomb core tensile failure regime. This offset increases as  $\bar{h}$  decrease. This chart elucidate that for same sandwich beam parameters ( $\bar{c}$  and  $\bar{h}$ ) auxetic core is less likely to face the tensile failure than hexagonal honeycomb core at any blast impulse load  $\bar{I}$ .

Comparison between Re-entrant honeycomb core and pyramidal core can be made by using Fig. 3.9.

Inverse design chart are also important and being used in industries to obtain the parameters based on the desired output. In Fig.3.8 the inverse design problem of sandwich beam with auxetic core under water blast have been addressed. Core parameters are  $\bar{\rho}=0.1$ ,  $\epsilon_Y=0.2$  and  $\epsilon_D=0.5$ . Contours of blast impulse  $\bar{I}$  is plotted for a pre-specified deflection  $\bar{w}=0.1$  and  $\bar{\psi} = 2 \times 10^{-3}$ . The axes are sandwich beam parameters  $\bar{c}$  and  $\bar{h}$ . The contours of non-dimensional mass  $\bar{M}$  is included in the chart in order to consider the mass as well while designing the sandwich beam for maximum blast impulse to be sustained. The design chart reveals that for a given mass  $\bar{M}$  the geometry in which face sheet thickness is negligible with respect to the core thickness maximizes the impulse. This observation supports the Taylor results which says that  $\bar{I}_{trans} \rightarrow 0$  as thickness of face sheet  $\bar{h} \rightarrow 0$ .

The maximum blast impulse sustained by the optimal geometries of five different cores have been plotted in Fig. 3.9. The constrain in the analysis is the given over non-dimensional mass  $\bar{M}$ . Where

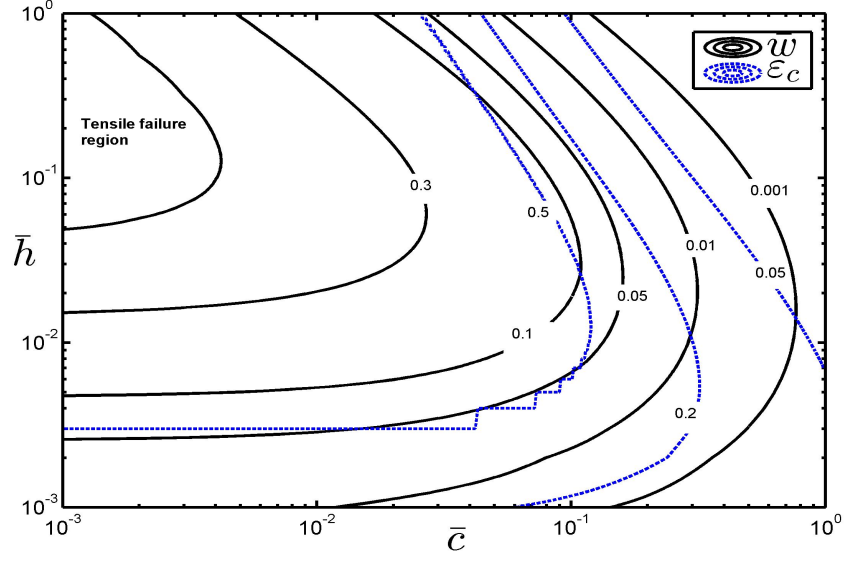


Figure 3.5: Design chart including contours of  $\bar{w}$  and  $\epsilon_c$  for a sandwich beam with an auxetic core of parameters  $\bar{\rho}=0.1, 0.002, \epsilon=0.5$ , subjected to a water blast ( $\bar{I} = 10^{-2}$  and  $\bar{\psi} = 2e^3$ )

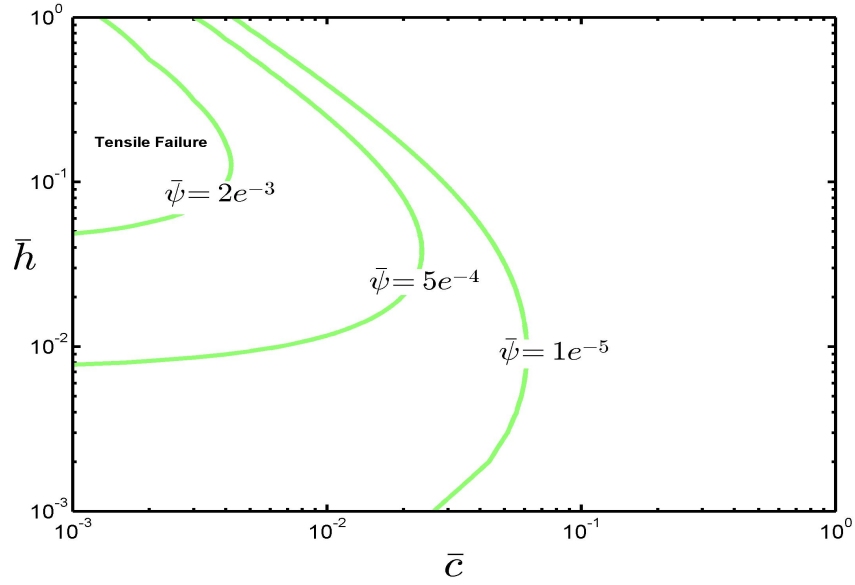


Figure 3.6: The tensile failure regime variation with respect to non-dimensional fluid structure interaction parameter  $\bar{\psi}$  for sandwich beam with auxetic core ( $\bar{\rho}=0.1, \epsilon_y=0.002, \epsilon_D=0.5$ ) under  $\bar{I} = 10^{-2}$ .

$\bar{M}$  is defined as given in Eq. 3.4 and  $M$  is the mass per unit width of the sandwich beam.

$$\bar{M} = \frac{M}{\rho_f L^2} = 2(2\bar{h}\bar{c} + \bar{c}\bar{\rho}) \quad (3.4)$$

From Fig. 3.9 it can be concluded that auxetic outperform all other conventional core topologies



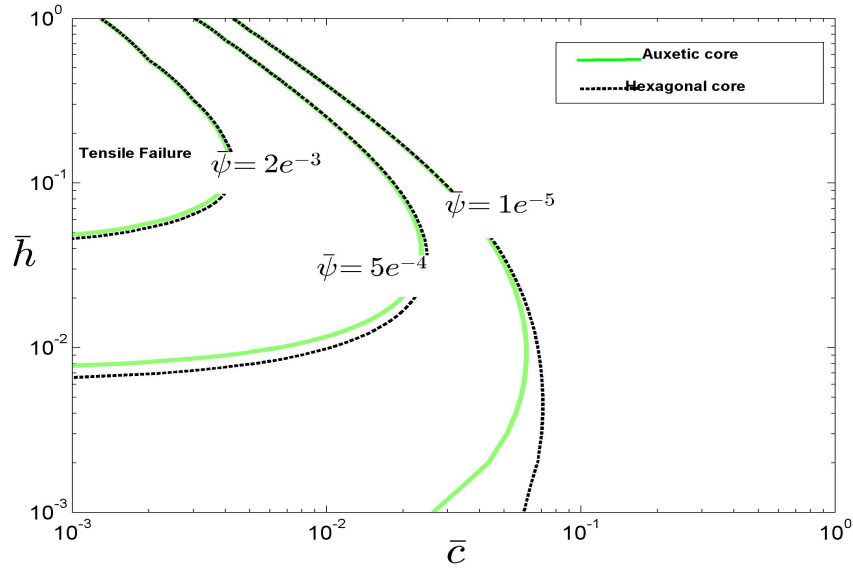


Figure 3.7: Comparison between re-entrant hexagonal auxetic core and Hexagonal core in terms of variation tensile failure regime with respect to non-dimensional fluid structure interaction parameter  $\bar{\psi}$

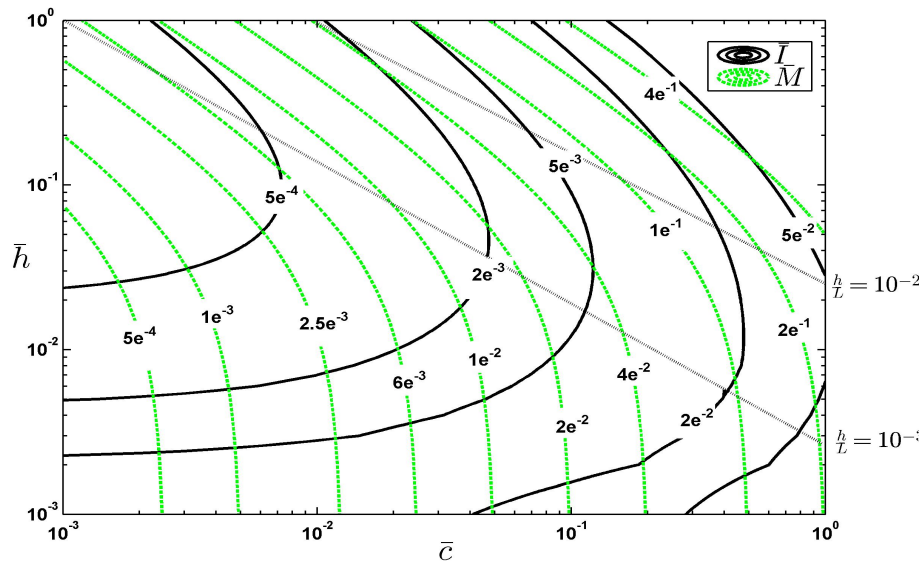


Figure 3.8: Inverse design chart for a sandwich beam, with a re-entrant hexagonal auxetic core ( $\bar{\rho}=0.1$ ,  $\epsilon_y=0.002$ ,  $\epsilon_D=0.5$ ), subjected to a water blast. The beam deflection is  $\bar{w}=0.1$  and the fluid-structure interaction parameter is taken as  $\psi = 2 \times 10^{-3}$ . Contours of  $\bar{T}$  and  $\bar{M}$  are displayed. The dotted lines trace the paths of selected values of  $\frac{h}{L}$

except the ideal core.

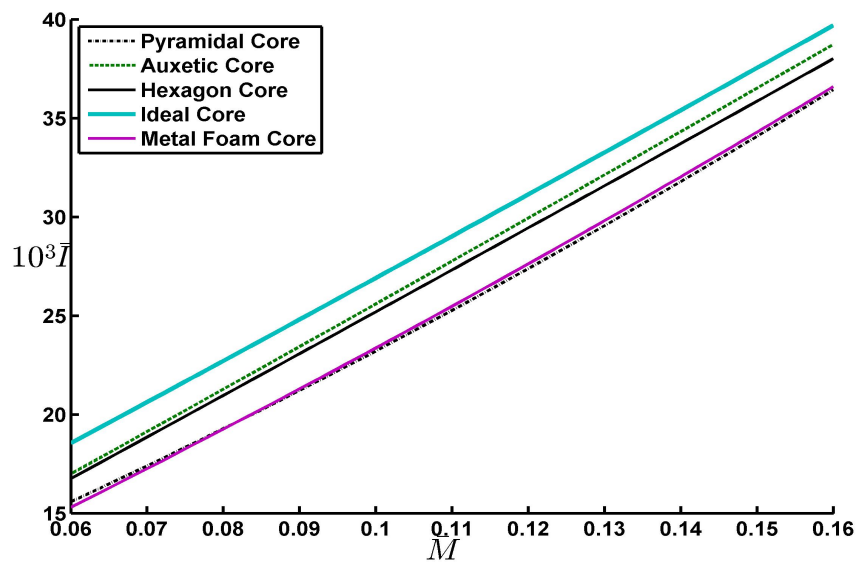


Figure 3.9: Comparison between major sandwich beam cores including re-entrant auxetic core in terms of maximum blast impulse sustained by optimal design of their respective sandwich beams

## Chapter 4

# Mechanics of Re-entrant Hexagonal Honeycomb

### 4.1 Introduction

Polymer, metal and ceramic honeycombs are used in variety of applications. Polymer and metal honeycombs are used as the cores of sandwich panels as an energy absorbing component in several application. For any material used as load bearing structure, an understanding of their mechanical behavior is important. Previous study on blast resistance of sandwich beams comprising re-entrant auxetic (Chapter 2) showed that re-entrant hexagonal auxetic core outperforms major conventional cores. Furthermore, studying 2D re-entrant hexagonal would help in understanding the mechanics of much more complex three dimensional auxetic foams.

The basic mechanics can be visualized from Fig. 1.9. Fig. 4.1 shows the re-entrant hexagonal honeycomb. We would like to understand its response when the load is applied in the plane  $X_1 - X_2$ . When a re-entrant honeycomb is compressed, the cell walls behaves as a beam and start to bend

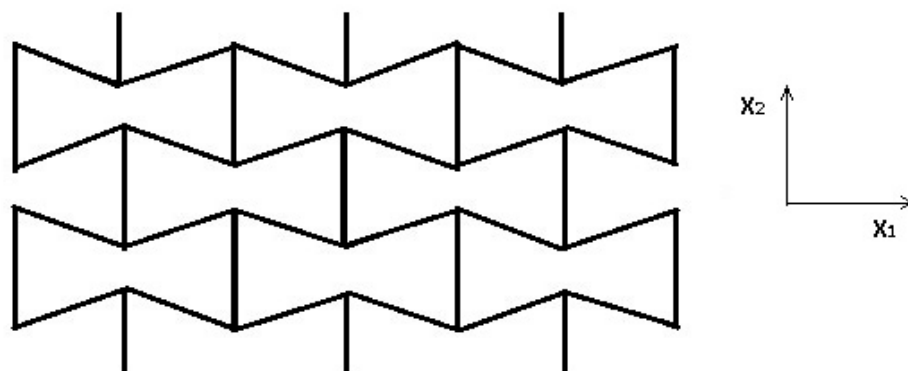


Figure 4.1: A re-entrant hexagonal cell honeycomb.

due to linear elastic deformation. Beyond a critical strain the cells collapses due to yielding, creep

or brittle fracture, depending on the nature of the cell wall material. Whenever the opposite cell walls contact each other, cell collapse ends. As the cells close up, the structure gets densified and its stiffness increases rapidly. The in-plane stiffness and strength are lowest because the cell walls respond to external loads by bending, and subsequent buckling, yielding, or fracturing. The out-of-plane (as shown in Fig. 4.1) stiffness and strength are much larger since they require axial deformation of the cell walls [32]. In this chapter, we are studying the in-plane response of 2D re-entrant hexagonal honeycombs.

## 4.2 In-plane Properties of Re-entrant Hexagon: Uni-axial loading

A unit cell of a hexagonal honeycomb is shown in Fig. 4.2. Regular hexagons (the sides are equal and the angles are all  $120^\circ$ ) with all cell walls of the same thickness possess isotropic in-plane properties as examined by Lorna et. al. [32]. A regular hexagon structure has two independent elastic moduli (a Young's modulus  $E$  and a shear modulus  $G$ ) and a single value of the yield stress,  $\sigma$ . However, for re-entrant hexagon or when the thickness of the walls regular hexagon is not constant, properties are anisotropic and the structure has five elastic constants ( $E_1, E_2, G_{12}, \nu_{12}$  and  $\nu_{21}$ ) and two value of yield stress  $\sigma_{Y1}$  and  $\sigma_{Y2}$ . However, there are only four independent elastic constant as reciprocal theorem (Eq. 4.1) needs to be satisfied.

$$E_1\nu_{12} = E_2\nu_{21} \quad (4.1)$$

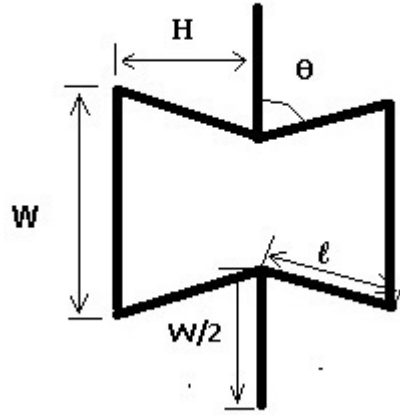


Figure 4.2: Re-entrant hexagonal unit cell and its parameters

Re-entrant honeycomb is a cellular solid and single most important characteristic of a cellular solid is its relative density,  $\rho^*/\rho_s$  ( $\rho^*$ , the density of cellular solid divided by parent material density,  $\rho_s$ ). It is also called the packing fraction of the cellular solid [32]. Typically, the mechanical properties of a cellular solid are related with its packing fraction. The packing fraction of the representative

unit cell of re-entrant honeycomb can be expressed by simple geometric analysis  $\rho^*/\rho^s$  [58], as given below :

$$\text{Relative density } (\bar{\rho}) = \frac{\text{volume of solid in unit cell}}{\text{Volume of unit cell}}$$

$$\bar{\rho} = \rho^*/\rho_s = \frac{\frac{t}{H}(\frac{W}{H} \sin(\theta) + 2)}{2(\frac{W}{H} \sin(\theta) - \cos(\theta))} \quad (4.2)$$

Non-dimensional representation of relative density in terms of parameters  $\bar{t}$ ,  $\bar{W}$  is;

$$\rho^*/\rho_s = \frac{\bar{t}(\bar{W} \sin(\theta) + 2)}{2(\bar{W} \sin(\theta) - \cos(\theta))} \quad (4.3)$$

Where,

$$\bar{t} = \frac{t}{H}, \bar{W} = \frac{W}{H}$$

#### 4.2.1 Linear Elastic Deformation

A re-entrant honeycomb, loaded in the  $X_1$  or  $X_2$  direction, deforms in a linear-elastic way and its cell walls bends. The Young's moduli in each direction are calculated by cellular material theory (i.e. cell wall bending model) [32] as explained below.

A re-entrant honeycomb loaded in  $X_1$  direction deforms as shown in Fig. 4.3 below :

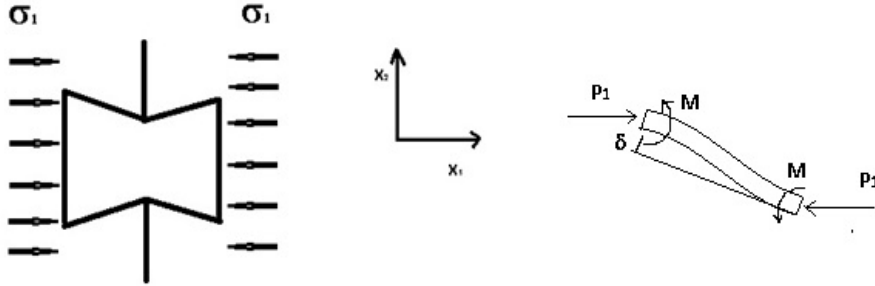


Figure 4.3: Cell deformation by cell wall bending, giving linear-elastic extension and compression of the honeycomb due to load in  $X_1$  direction

As re-entrant cell is symmetric about both  $X_1$  and  $X_2$  axis, we are considering only the part of unit cell in second quadrant here.

$$P_1 = \sigma_1(W - l \cos(\theta)) \quad (4.4)$$

$$M_1 = \frac{P_1 l \cos(\theta)}{2} \quad (4.5)$$

Resultant deflection in the beam is because of force  $P_1$  and moment  $M_1$  as

$$\delta = \delta_p - \delta_M \quad (4.6)$$

Where  $\delta_p$  corresponds to deflection due to  $P_1$  and  $\delta_M$  corresponds to deflection due to  $M_1$

$$\delta_P = \frac{P_1 l^3 \cos(\theta)}{3E_s I}, \delta_M = \frac{P_1 l^3 \cos(\theta)}{4E_s I} \quad (4.7)$$

Generalized strain  $\varepsilon_2$  and Young's modulus  $E_2^*$  in  $X_1$  are as given in Eq. 4.8 and Eq. 4.9, respectively

$$\varepsilon_1 = \frac{\delta \sin(\theta)}{l \cos(\theta)} = \frac{\sigma_1 (W - l \cos(\theta)) b l^2 \cos^2 \theta}{12 E_s I \sin(\theta)} \quad (4.8)$$

The Young's modulus in  $X_1$  direction is  $E_1^* = \frac{\sigma_1}{\varepsilon_1}$

$$E_1^* = \frac{\sigma_1}{\varepsilon_1} = \left(\frac{t}{l}\right)^3 \frac{\sin(\theta) E_s}{\left(\frac{W}{l} - \cos(\theta)\right) \cos^2 \theta} \quad (4.9)$$

Similarly for loading in  $X_2$  direction generalized strain  $\varepsilon_2$  and Young's modulus  $E_2^*$  in  $X_2$  direction are as given in Eq. 4.10 and Eq. 4.11, respectively

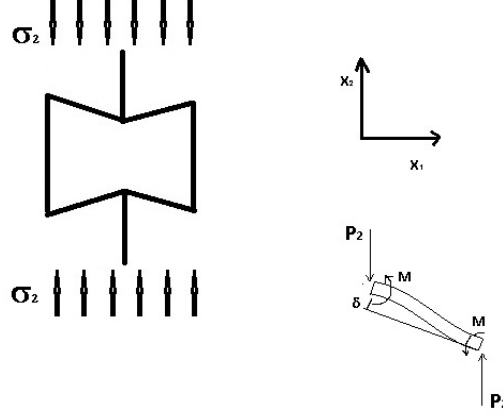


Figure 4.4: Cell deformation by cell wall bending, giving linear-elastic extension and compression of the honeycomb due to load in  $X_2$  direction

$$\varepsilon_2 = \frac{\sigma_2 (W - l \cos(\theta)) b l^3 \sin^3 \theta}{12 E_s I (W - l \cos(\theta))} \quad (4.10)$$

$$E_2^* = \frac{\sigma_2}{\varepsilon_2} = \left(\frac{t}{l}\right)^3 \frac{(W/l - \cos \theta) E_s}{\sin^3 \theta} \quad (4.11)$$

The Poisson's ratios are calculated by taking negative ratio of strain in the normal direction to the strain in parallel direction with respect to the loading.

$$\nu_{12}^* = -\frac{\varepsilon_2}{\varepsilon_1} \quad (4.12)$$

$$\nu_{12}^* = -\frac{\sin^2 \theta}{\left(\frac{W}{l} - \cos \theta\right) \cos \theta} \quad (4.13)$$

Similarly,

$$\vartheta_{21}^* = -\frac{\varepsilon_1}{\varepsilon_2} \quad (4.14)$$

$$\vartheta_{21}^* = -\frac{\left(\frac{W}{l} - \cos \theta\right) \cos \theta}{\sin^2 \theta} \quad (4.15)$$

Note that, either one of  $\vartheta_{12}^*$  and  $\vartheta_{21}^*$  also can be find out using reciprocal theorem (Eq. 4.1). To find the fourth independent component of 2D orthotropic material, namely  $G_{12}$  shear modulus, we performed a shear deformation analysis on re-entrant hexagonal auxetic cells as shown in Fig. 4.5.

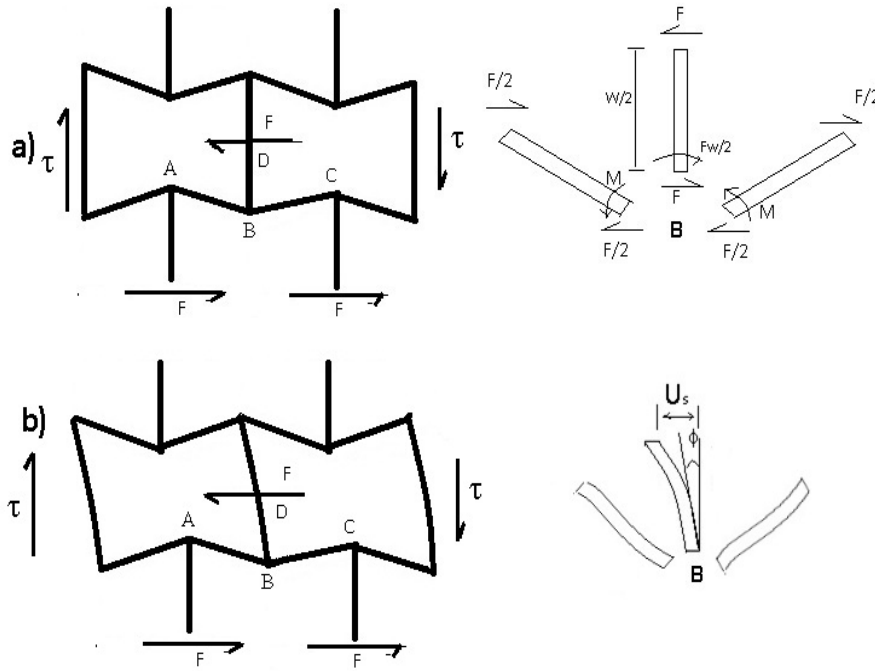


Figure 4.5: Schematic of re-entrant hexagonal auxetic cell under shear deformation (a) Undeformed configuration (b) Deformed configuration

Considering re-entrant hexagonal auxetic part ABCD in Fig. 4.5. When the re-entrant honeycomb is sheared; the deflection  $U_s$  occurs because of bending of beam BD and its rotation about the point B. Summing moment at B gives us the moment  $M$  in beams AB and BC (Eq. 4.16).

$$2M = \frac{Fw}{2} \quad (4.16)$$

$$\Rightarrow M = \frac{Fw}{4} \quad (4.17)$$

Beams AB and BC simply rotates about point B as they are symmetric about  $X_2$  direction, without any relative deformation. Using a standard solution of problem of beam under pin-pin boundary

conditions and a moment  $M$  applied at both end as shown in Fig. 4.6, we get

$$\phi = \frac{Fwl}{24E_s I} \quad (4.18)$$

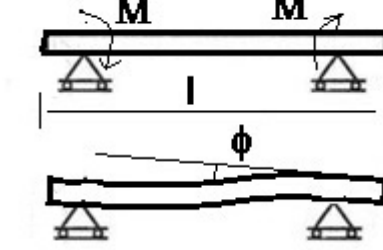


Figure 4.6: A beam under pin-pin boundary condition and pure bending

Standard deflection expression for problem in Fig. 4.6 is:

$$\phi = \frac{ML}{6EI} \quad (4.19)$$

Where,  $E$  is Young's modulus and  $I$  is moment of inertia of beam. The deflection  $U_s$  of point D with respect to B is:

$$U_s = \frac{1}{2}\phi w + \frac{F}{3E_s I} \left(\frac{w}{2}\right)^3 \quad (4.20)$$

Shear strain,  $\gamma$ , is given by:

$$\gamma = \frac{2U_s}{w - l \cos \theta} \quad (4.21)$$

$$\Rightarrow \gamma = \frac{Fw^2}{24E_s I} \left(\frac{l + 2w}{w - l \cos \theta}\right) \quad (4.22)$$

Using the shear stress,  $\tau$ , the  $G_{12}$  for auxetic cell results as:

$$\tau = \frac{F}{2lb \cos \theta} \quad (4.23)$$

$$G = \frac{\tau}{\gamma} \quad (4.24)$$

$$G_{12} = \left(\frac{t}{l}\right)^3 \frac{E_s \left(\frac{w}{l} - \cos \theta\right)}{\left(\frac{w}{l}\right)^2 \left(1 + \frac{2w}{l}\right) \sin \theta} \quad (4.25)$$

## 4.2.2 Plastic Collapse

Honeycombs made of metals and few polymers, collapses plastically when the bending moment in the cell walls reaches the fully plastic moment. A stress-strain curve with a plateau will be generated both in compression and in tension at the plastic collapse stress level  $\sigma_{pl}$ . Formulation of plastic collapse stress for re-entrant hexagonal honeycomb cell is given below.



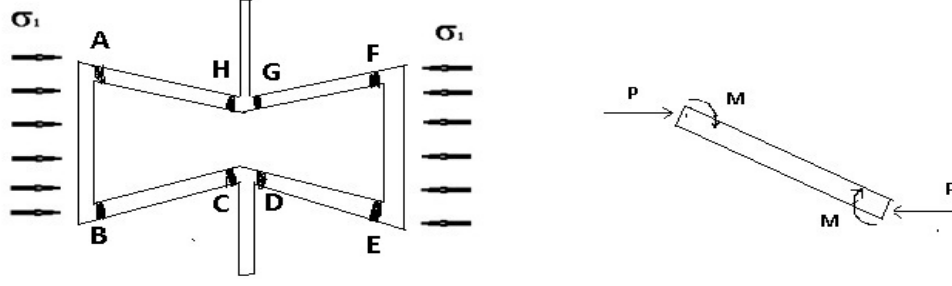


Figure 4.7: Plastic hinge formation when load is applied in  $X_1$  direction

From Fig. 4.7 force  $P$ , and moment  $M$ , is given as expressions in Eq. 4.26 and Eq. 4.27, respectively.

$$P = \sigma(W - l \cos(\theta))b \quad (4.26)$$

$$M = \frac{Pl \cos(\theta)}{2} \quad (4.27)$$

Plastic moment  $M_p$  for a beam is given as Eq. 4.28.

$$M_p = \frac{bt^2}{4} \sigma_{ys} \quad (4.28)$$

During a plastic rotation  $\phi$  of the four plastic hinges A, B, C, and H the plastic work done at the hinges can be obtained by an upper bound of work done in Eq. 4.29.

$$4M_p \geq 2\sigma(W - l \cos(\theta))l \cos(\theta) \quad (4.29)$$

where  $M_p$  is the fully plastic moment of the cell wall in bending. From Eq. 4.28 and Eq. 4.29, we get

$$\frac{\sigma_{pl}}{\sigma_{ys}} = \frac{\bar{t}^2}{2} \left( \frac{1}{2(\frac{W}{\bar{t}} - \cos(\theta)) \cos(\theta)} \right) \quad (4.30)$$

where,  $\sigma_{pl}$  is the plastic collapse strength,  $\sigma_{ys}$  is the yield strength of parent material.

### 4.3 Corner Singularity of Re-entrant Wedge

Re-entrant angle in the auxetic structure gives rise to singularity at the tip. Here in this study we have speculate that singularity would be same as the standard infinite wedge problem. Williams developed a method of exploring the nature of the stress field near this singularity by defining a set of polar coordinates centered on the corner and expanding the stress field as an asymptotic series in powers of  $r$ .

We are concerned only with the stress components in the notch at very small values of  $r$  and hence we imagine looking at the corner through a strong microscope, so that we see the wedge of Figure 4.8 with 'loading at infinity'.

$$\phi = r^{n+2} f(\theta) \quad (4.31)$$

$$\phi = r^{n+2} \{A_1 \cos(n+2)\theta + A_2 \cos n\theta + A_3 \sin(n+2)\theta + A_4 \sin n\theta\} \quad (4.32)$$

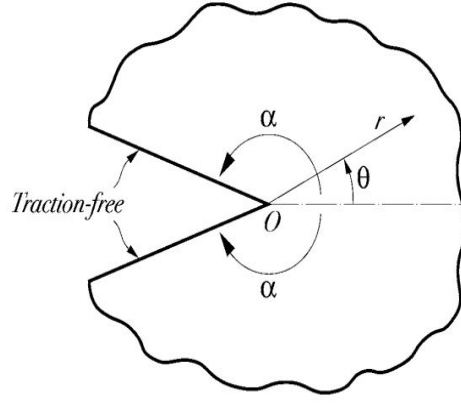


Figure 4.8: The semi-infinite notch

In William's notation, we replace  $n$  by  $(\lambda-1)$  in Eq. 4.32, Obtaining the stress function

$$\phi = r^{\lambda+1} \{A_1 \cos(\lambda+1)\theta + A_2 \cos(\lambda-1)\theta + A_3 \sin(\lambda+1)\theta + A_4 \sin(\lambda-1)\theta\} \quad (4.33)$$

Which lead to stress components as

$$\sigma_{rr} = r^{\lambda-1} \{-A_1 \lambda(\lambda-1) \cos(\lambda+1)\theta - A_2 \lambda(\lambda-3) \cos(\lambda-1)\theta - A_3 \lambda(\lambda+1) \sin(\lambda+1)\theta - A_4 \lambda(\lambda-3) \sin(\lambda-1)\theta\} \quad (4.34)$$

$$\sigma_{r\theta} = r^{\lambda-1} \{A_1 \lambda(\lambda+1) \sin(\lambda+1)\theta + A_2 \lambda(\lambda-1) \sin(\lambda-1)\theta - A_3 \lambda(\lambda+1) \cos(\lambda+1)\theta - A_4 \lambda(\lambda-1) \cos(\lambda-1)\theta\} \quad (4.35)$$

$$\sigma_{\theta\theta} = r^{\lambda-1} \{A_1 \lambda(\lambda+1) \cos(\lambda+1)\theta + A_2 \lambda(\lambda+1) \cos(\lambda-1)\theta + A_3 \lambda(\lambda+1) \sin(\lambda+1)\theta + A_4 \lambda(\lambda+1) \sin(\lambda-1)\theta\} \quad (4.36)$$

For this solution to satisfy the traction-free boundary conditions

$$\sigma_{r\theta} = \sigma_{\theta\theta} = 0; \theta = \pm\alpha \quad (4.37)$$

$$\lambda[A_1(\lambda+1) \sin(\lambda+1)\alpha + A_2(\lambda-1) \sin(\lambda-1)\alpha - A_3(\lambda+1) \cos(\lambda+1)\alpha - A_4(\lambda-1) \cos(\lambda-1)\alpha] = 0 \quad (4.38)$$

$$\lambda[-A_1(\lambda+1) \sin(\lambda+1)\alpha - A_2(\lambda-1) \sin(\lambda-1)\alpha - A_3(\lambda+1) \cos(\lambda+1)\alpha - A_4(\lambda-1) \cos(\lambda-1)\alpha] = 0 \quad (4.39)$$

$$\lambda[A_1(\lambda+1) \cos(\lambda+1)\alpha + A_2(\lambda+1) \cos(\lambda-1)\alpha + A_3(\lambda+1) \sin(\lambda+1)\alpha + A_4(\lambda+1) \sin(\lambda-1)\alpha] = 0 \quad (4.40)$$

$$\lambda[A_1(\lambda+1) \cos(\lambda+1)\alpha + A_2(\lambda+1) \cos(\lambda-1)\alpha - A_3(\lambda+1) \sin(\lambda+1)\alpha - A_4(\lambda+1) \sin(\lambda-1)\alpha] = 0 \quad (4.41)$$

Since all the equations have a  $\lambda$  multiplier,  $\lambda = 0$  must be an eigenvalue for all wedge angles. Non-trivial solution exists for the above homogeneous equation at only certain eigen values,  $\lambda$ . Simplifying equations 4.38 – 4.41 we get

$$A_1(\lambda+1) \sin(\lambda+1)\alpha + A_2(\lambda-1) \sin(\lambda-1)\alpha = 0 \quad (4.42)$$

$$A_1(\lambda+1) \cos(\lambda+1)\alpha + A_2(\lambda+1) \cos(\lambda-1)\alpha = 0 \quad (4.43)$$

$$A_3(\lambda+1) \cos(\lambda+1)\alpha + A_4(\lambda-1) \sin(\lambda-1)\alpha = 0 \quad (4.44)$$

$$A_3(\lambda+1) \sin(\lambda+1)\alpha + A_4(\lambda+1) \sin(\lambda-1)\alpha = 0 \quad (4.45)$$

Above equation leads two independent matrix equations as given below

$$\begin{bmatrix} (\lambda+1) \sin(\lambda+1)\alpha & (\lambda-1) \sin(\lambda-1)\alpha \\ (\lambda-1) \cos(\lambda+1)\alpha & (\lambda-1) \cos(\lambda-1)\alpha \end{bmatrix} \begin{Bmatrix} A_1 \\ A_2 \end{Bmatrix} = 0 \quad (4.46)$$

$$\begin{bmatrix} (\lambda+1) \cos(\lambda+1)\alpha & (\lambda-1) \cos(\lambda-1)\alpha \\ (\lambda+1) \sin(\lambda+1)\alpha & (\lambda+1) \sin(\lambda-1)\alpha \end{bmatrix} \begin{Bmatrix} A_3 \\ A_4 \end{Bmatrix} = 0 \quad (4.47)$$

For a non-trivial solution of symmetric terms  $A_1$  and  $A_2$  which corresponds to Mode-I, the determinant of co-efficient matrix (4.46) must be zero. The characteristic equation using the non-trivial solution condition is

$$\lambda \sin 2\alpha + \sin(2\lambda\alpha) = 0 \quad (4.48)$$

Similarly characteristic equation for non-trivial solution of antisymmetric terms  $A_3$  and  $A_4$  corresponding to Mode-II is

$$\lambda \sin 2\alpha - \sin(2\lambda\alpha) = 0 \quad (4.49)$$

#### 4.4 Direct stiffness methods using frame element

In this section, we employ direct stiffness matrix method on re-entrant hexagon auxetic element using frame element.

A frame element is formulated to model a straight bar of any arbitrary cross-section, which can deform not only in the axial direction but also in the directions perpendicular to the axis of the bar. The bar is capable of carrying both axial and transverse forces, as well as moments there for has three degree of freedoms. A frame element possess the properties of both truss and beam elements. In fact the frame structure can be found in most of our real world structural problems. There are not many structures that deforms and carry loadings purely in axial directions or purely in transverse directions.

Here, we consider the re-entrant hexagon element as a frame structure divided into frame elements connected by nodes. Each element has two nodes and of beam element length  $l_e$ . The elements and nodes are numbered separately in a convenient manner as shown in Fig. 4.9. In a planar frame element, there are three degrees of freedom (DOFs) at one node in its local coordinate system namely, axial deflection in the  $x$  direction,  $u$ ; deflection in the  $y$  direction,  $v$ ; and the rotation in the  $x - y$  plane with respect to  $z$ -axis,  $\theta$ .

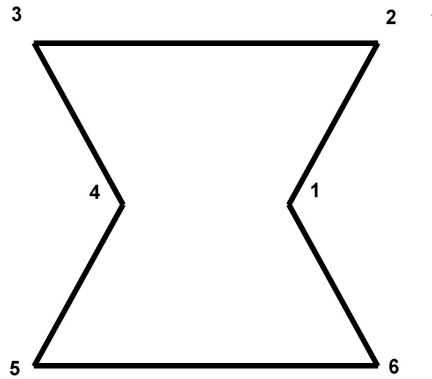


Figure 4.9: Re-entrant hexagon auxetic element node numbering

Equations for a frame element in local coordinates as shown in Fig. can be given as followings.

Element frame displacement vector is taken as

$$d_e = \begin{Bmatrix} d_1 \\ d_2 \\ d_3 \\ d_4 \\ d_5 \\ d_6 \end{Bmatrix} = \begin{Bmatrix} u_1 \\ v_1 \\ \theta_1 \\ u_2 \\ v_2 \\ \theta_2 \end{Bmatrix} \quad (4.50)$$

Where,  $u_1, v_1, \theta_1$  are displacement component of node 1 and  $u_2, v_2, \theta_2$  are displacement component of node 2. Stiffness matrix of a frame element  $k^{Frame}$  is a combination of stiffness matrix of truss  $k^{Truss}$  and stiffness matrix of a beam  $k^{Beam}$  as shown in Eq. 4.51.

$$K^{Frame} = K^{Truss} + K^{Beam} \quad (4.51)$$

The stiffness matrix of truss element after extending it to corresponding order of DOFs in 6x6 frame element stiffness matrix is given as

$$K_e^{truss} = \begin{bmatrix} \frac{AE}{L} & 0 & 0 & -\frac{AE}{L} & 0 & 0 \\ 0 & 0 & 0 & 0 & 0 & 0 \\ 0 & 0 & 0 & 0 & 0 & 0 \\ -\frac{AE}{L} & 0 & 0 & \frac{AE}{L} & 0 & 0 \\ 0 & 0 & 0 & 0 & 0 & 0 \\ 0 & 0 & 0 & 0 & 0 & 0 \end{bmatrix} \quad (4.52)$$

Similarly, the stiffness matrix of beam element after extending to corresponding order of DOFs in 6X6 frame element stiffness matrix is given as

$$K_e^{beam} = \begin{bmatrix} 0 & 0 & 0 & 0 & 0 & 0 \\ 0 & \frac{12EI}{L^3} & \frac{6EI}{L^2} & 0 & -\frac{12EI}{L^3} & \frac{6EI}{L^2} \\ 0 & \frac{6EI}{L^2} & \frac{4EI}{L} & 0 & -\frac{6EI}{L^2} & \frac{2EI}{L} \\ 0 & 0 & 0 & 0 & 0 & 0 \\ 0 & -\frac{12EI}{L^3} & -\frac{6EI}{L^2} & 0 & \frac{12EI}{L^3} & -\frac{6EI}{L^2} \\ 0 & \frac{6EI}{L^2} & \frac{2EI}{L} & 0 & -\frac{6EI}{L^2} & \frac{4EI}{L} \end{bmatrix} \quad (4.53)$$

The two matrices in Eq. 4.52 and 4.53 are now superimposed together to obtain the stiffness matrix for the frame element:

$$K_e^{frame} = \begin{bmatrix} \frac{AE}{L} & 0 & 0 & -\frac{AE}{L} & 0 & 0 \\ 0 & \frac{12EI}{L^3} & \frac{6EI}{L^2} & 0 & -\frac{12EI}{L^3} & \frac{6EI}{L^2} \\ 0 & \frac{6EI}{L^2} & \frac{4EI}{L} & 0 & -\frac{6EI}{L^2} & \frac{2EI}{L} \\ -\frac{AE}{L} & 0 & 0 & \frac{AE}{L} & 0 & 0 \\ 0 & -\frac{12EI}{L^3} & -\frac{6EI}{L^2} & 0 & \frac{12EI}{L^3} & -\frac{6EI}{L^2} \\ 0 & \frac{6EI}{L^2} & \frac{2EI}{L} & 0 & -\frac{6EI}{L^2} & \frac{4EI}{L} \end{bmatrix} \quad (4.54)$$

To assemble the individual frame element in global coordinates, coordination transformation 4.55

is used

$$T = \begin{bmatrix} l_x & m_x & 0 & 0 & 0 & 0 \\ l_y & m_y & 0 & 0 & 0 & 0 \\ 0 & 0 & 1 & 0 & 0 & 0 \\ 0 & 0 & 0 & l_x & m_x & 0 \\ 0 & 0 & 0 & l_y & m_y & 0 \\ 0 & 0 & 0 & 0 & 0 & 1 \end{bmatrix} \quad (4.55)$$

Where  $l_x$ ,  $m_x$ ,  $l_y$ ,  $m_y$  are direction cosines of local coordinates system w.r.t. global coordinates, given as

$$\begin{aligned} l_x &= \frac{X_j - X_i}{l_e} = \cos \theta, m_x = \frac{Y_j - Y_i}{l_e} \\ l_y &= \cos \theta = -\sin \theta = \frac{Y_j - Y_i}{l_e} \\ m_y &= \cos \theta = \frac{X_j - X_i}{l_e} \end{aligned} \quad (4.56)$$

## 4.5 Configuration Forces in Re-entrant Hexagonal Auxetic

Classical Newtonian forces describes the response of a body to deformation using balance laws of linear and angular momentum. Configurational forces are additionally needed to understand the phenomenon associated with material itself. Importance of these forces clarified more after the work of Eshelby [59] on lattice defects and force on singularities [60]. Configurational forces are essentially driving for to move a defect. In re-entrant hexagonal auxetic cell, the re-entrant angle acts as a defect and we speculate that there would be always a pseudo force  $Q$ , acting on the re-entrant corner to take back the re-entrant cell to the equilibrium.

In this section we derive an expression for configuration force generated in a re-entrant hexagonal auxetic cell under a compressive load. It implies to the force required to open up the re-entrant angle completely. The re-entrant hexagonal auxetic unit cell is shown in Fig. 4.10. When this is subjected to a uniform compression load a pseudo force  $Q$  will be generated as given by the expression in Eq. 4.57.

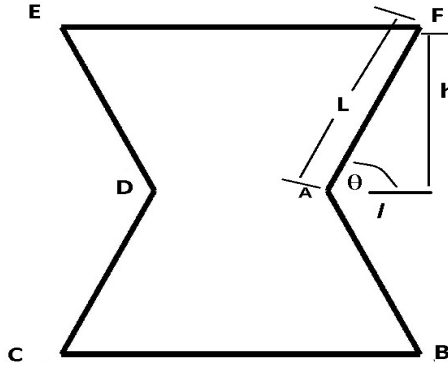


Figure 4.10: Re-entrant hexagonal unit cell

$$Q = -\frac{\partial \Pi}{\partial l} \quad (4.57)$$

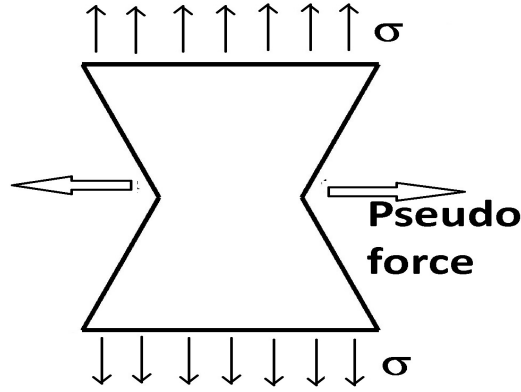


Figure 4.11: Configuration force in re-entrant hexagonal auxetic

The relation in Eq. 4.60 given the expression of strain energy  $\pi$ . Where  $F$ ,  $P$  and  $H$  are the force component as shown in free body diagram of rib A-B in Fig. 4.12 and  $h$ ,  $l$  and  $L$  are re-entrant hexagonal auxetic unit cell parameters as shown in Fig. 4.10. Formulation of configuration force  $Q$  with respect to the parameter  $l$  is as following

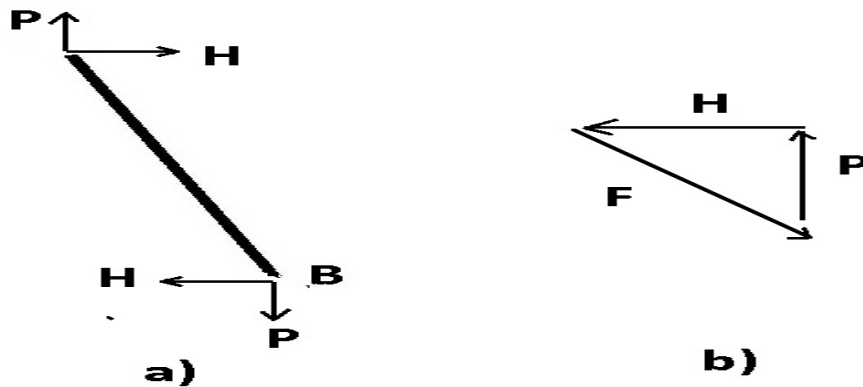


Figure 4.12: Free body diagram of forces in rib A-B

Configuration force generated at the re-entrant corner with respect to configurational parameter  $l$  can be given by

$$Q = -\frac{\partial \Pi}{\partial l} \quad (4.58)$$

Where,  $Q$  is the configurational force.

Strain energy is given by the Eq. 4.60 as given below

$$\Pi = \frac{1}{2} \frac{\sigma^2}{E} V \quad (4.59)$$

$$\Pi = \frac{1}{2} \frac{F^2}{A^2 E} AL \quad (4.60)$$

From free body diagram of a rib as shown in Fig. 4.12 above, we get

$$\frac{P}{H} = \tan \theta; \frac{P}{F} = \sin \theta; \frac{H}{F} = \cos \theta \quad (4.61)$$

$$\frac{h}{l} = \tan \theta; \frac{h}{L} = \sin \theta; \frac{l}{L} = \cos \theta \quad (4.62)$$

$$\begin{aligned} F^2 &= P^2 + H^2 \\ &= P^2(1 + \cot^2 \theta) \end{aligned} \quad (4.63)$$

$$\frac{dl}{L} = -\sin \theta d\theta \quad (4.64)$$

$$\frac{d\theta}{dl} = -\frac{\csc \theta}{L} \quad (4.65)$$

$$\begin{aligned} Q &= \frac{LP^2}{2AE} \frac{d}{d\theta} (1 + \cot^2 \theta) \frac{d\theta}{dl} \\ &= \frac{LP^2}{2AE} 2 \cot \theta (-) \csc^2 \theta \frac{d\theta}{dl} \\ &= \frac{LP^2}{AE} \cot \theta \frac{\csc^3 \theta}{L} \end{aligned} \quad (4.66)$$

$$\begin{aligned} Q(P, l) &= \frac{P^2}{AE} \frac{l}{h} \left( \frac{L}{h} \right)^3 \\ &= \frac{P^2}{AE} \frac{L^3 l}{h^4} \\ &= \frac{P^2}{AE} \frac{L^3 l}{(L^2 - l^2)^2} \end{aligned} \quad (4.67)$$

The configurational force  $Q$  is a function of applied load  $P$  and the parameter  $l$  as through the formulation in Eq. 4.67. It varies non-linearly with respect to the distance  $l$  for a given load  $P$  and quadratically with respect to the load  $P$  for a given distance  $l$ .



## Chapter 5

# Result and Discussions: Mechanics of Re-entrant Hexagonal Honeycomb

In this chapter the mechanics of re-entrant hexagonal honeycomb have been discussed based on the methodologies discussed in previous chapter.

### 5.1 In plane properties of re-entrant hexagonal structure

The generalized material constants calculated in the previous section can be used to obtain the compliance matrix and can be used in finite element analysis as well. As these generalized material constants depends upon the cell parameter we have plotted these parameters with respect to the re-entrant angle for different width to length ( $\frac{W}{l}$ ) ratios for a parent material of Young's modulus  $E_s = 120MPa$ .

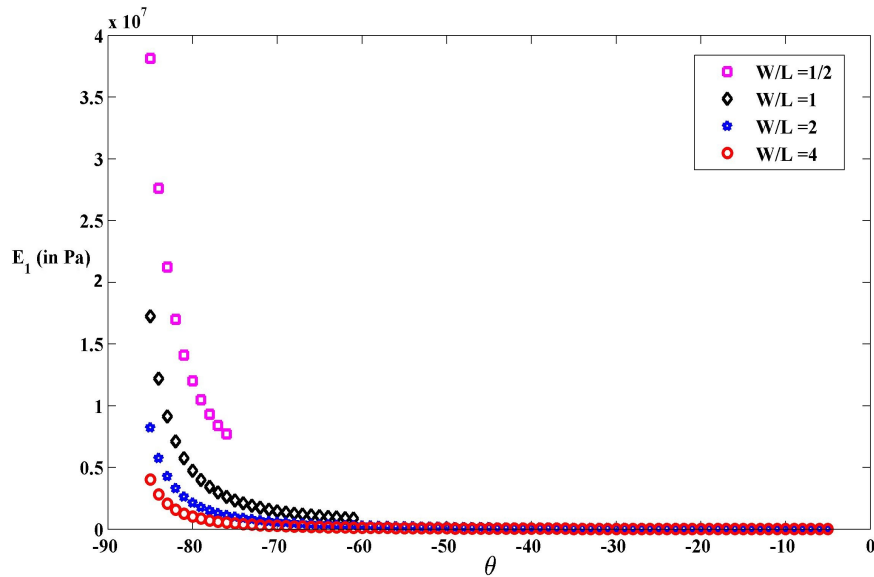


Figure 5.1: Variation of  $E_1$  vs  $\theta$  for re-entrant hexagon auxetic for different  $\frac{W}{l}$ .

Figure 5.1 includes the plots between generalized average Young's modulus  $E_1$  and re-entrant angle  $\theta$ . It shows that as the re-entrant angle goes towards  $90^\circ$ ,  $E_1$  increase which means that the slope of generalized stress-strain would increase with the increasing re-entrant angle  $\theta$ .

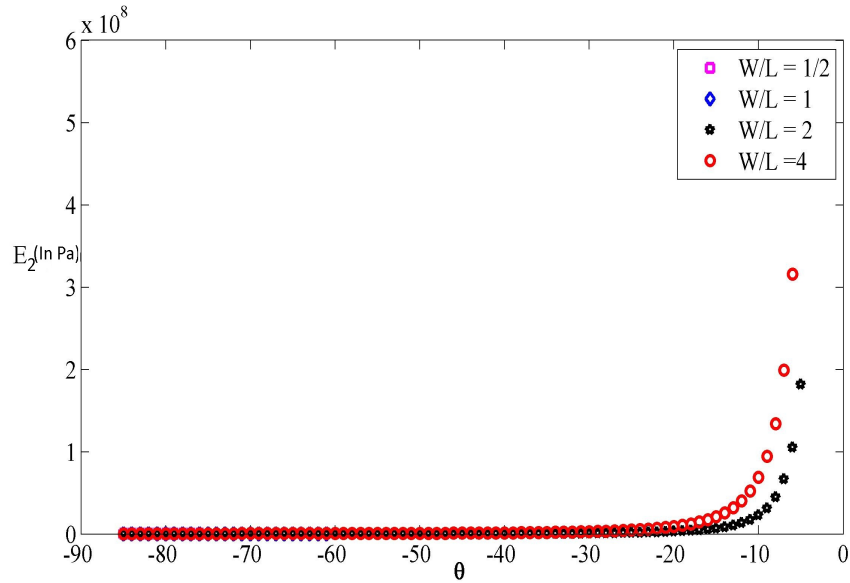


Figure 5.2: Variation of  $E_2$  vs.  $\theta$  for re-entrant hexagon auxetic for different  $\frac{W}{l}$

Opposite to  $E_1$  5.2, the Young's modulus in  $X_2$  direction the Young's modulus decreases as  $\theta$  increases implying that force required to open up the re-entrant angle would decrease with increasing  $\theta$ . This result even supports the study on configuration force balance in Sec. 4.5.

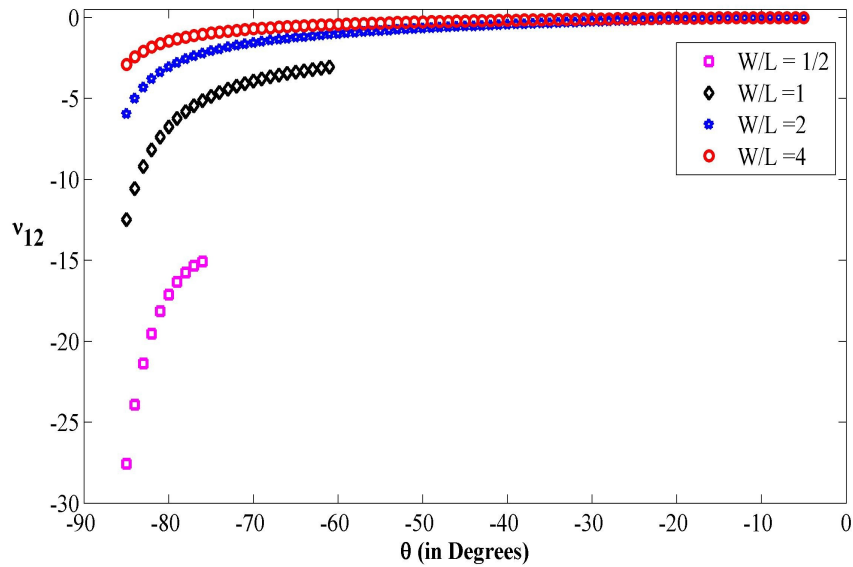


Figure 5.3: Variation of  $\nu_{12}$  vs  $\theta$  for re-entrant hexagon auxetic for different  $\frac{W}{l}$ .

The Poisson's ratio for this structure is negative. As discussed in introductory Sec. 1.1, ther-

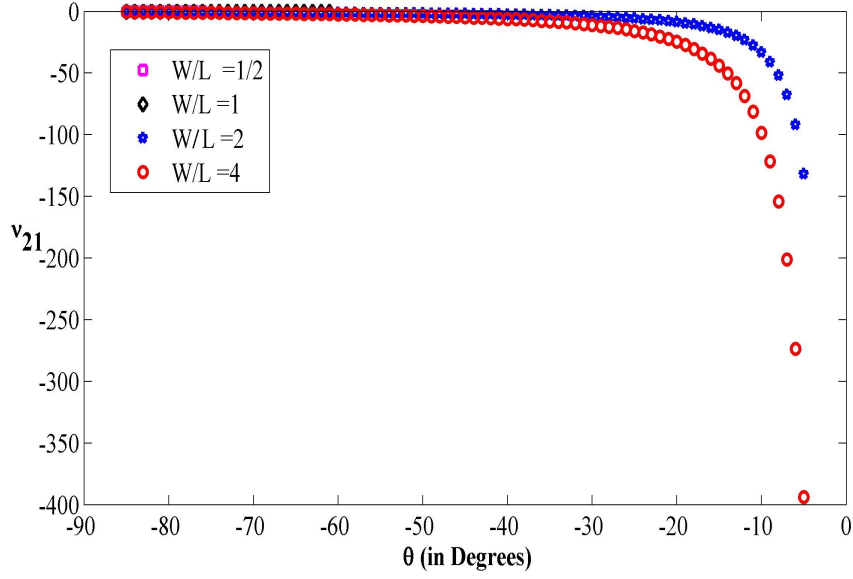


Figure 5.4: Variation of  $\nu_{21}$  vs  $\theta$  for re-entrant hexagon auxetic for different  $\frac{W}{L}$ .

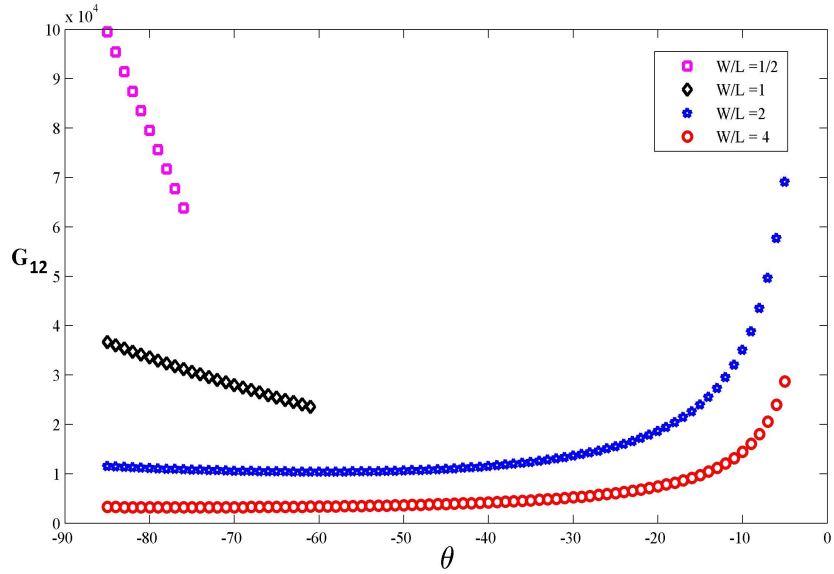


Figure 5.5: Variation of  $G_{12}$  vs  $\theta$  for re-entrant hexagon auxetic for different  $\frac{W}{L}$ .

modynamically Poisson's ratio is restricted  $-1 \leq \nu \leq 0.5$  for homogeneous isotropic materials. But structure of cellular solids enhances the Poisson's ratio, for example as shown in Fig. 5.3. As re-entrant angle opens up the Poisson's ratio,  $\nu_{12}$ , also keeps on increasing. Whereas,  $\nu_{21}$  from the definition is inverse of  $\nu_{12}$  that's why decreases with increasing re-entrant angle.

From Figs. 5.1-5.4, unequal number of data points in the graphs is because of the constraint applied over the re-entrant cell such that the re-entrant corners does not cross each other.

Equation 4.30 gives the plastic collapse strength in  $X_1$  direction. This equation provides the analytical expression for the first study result where we determined the plastic collapse strength of

re-entrant hexagonal auxetic using finite element analysis. Typically mechanical behavior of cellular solid depends upon its packing factor, also known as relative density  $\bar{\rho}$ . Relative density of re-entrant hexagonal honeycomb representative unit cell is given in Eq. 4.3 in terms of its non-dimensional geometrical parameters.

Validation of the auxetic compliance matrix (Eq. 5.1) is done by employing finite element analysis using the generalized elastic constants found here. A 2D rectangular structure representing a re-entrant auxetic cell of width to length ratio,  $\frac{w}{l}$ , equals to unity, thickness to length ratio,  $\frac{t}{l}$ , equals to 0.1 and with a re-entrant angle  $\theta = 75^\circ$ , is modelled with a compressive loading and symmetric boundary condition across X axis, as shown in Fig. 5.6.

$$D = \begin{bmatrix} \frac{1}{E_1} & -\frac{\nu_{21}}{E_2} & 0 \\ -\frac{\nu_{12}}{E_2} & \frac{1}{E_2} & 0 \\ 0 & 0 & \frac{1}{G_{12}} \end{bmatrix} \quad (5.1)$$

Parent material as Aluminum is taken with Young's modulus of value  $E_s = 120MPa$ . The element used in FE modelling is CPS4R, 4-node bilinear plane stress quadrilateral with reduced integration. The displacement vector in  $X_2$  direction obtained through the finite element modelling is as shown in Fig. 5.7. The direction of displacement vector obtained through finite element modelling is shown

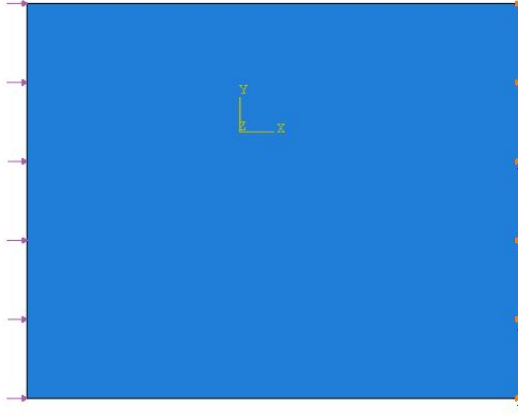


Figure 5.6: Loading and boundary conditions on a representative 2D rectangle ( $W = 30mm$ )

in Fig. 5.7.

Figure 5.7 shows that under a compressive loading in axial direction unlike a conventional material auxetic material contracts in lateral direction. Generalized compliance matrix obtained by CMT depicts negative Poisson's ratio behavior.

Variation of these elastic constants with the relative density is summarized in Fig. 5.8 for a re-entrant angle of  $75^\circ$  with width,  $W$ , equals to the length,  $l$ . It is observed that  $E_1$  and  $E_2$  varies cubically with relative density  $\bar{\rho}$ . Where as, both the Poisson's ratios  $\nu_{12}$  and  $\nu_{21}$  are independent of relative density because they only depends upon the deformations in orthogonal axes as shown in Fig. 5.8.

In literature typically  $\bar{\rho}$  is related to ratio of thickness to cellular rib length by fixing other geometrical parameters. For a re-entrant angle  $\theta = 72^\circ$  with  $\bar{w}=1$ , the plot in Fig. 5.9 compares the result obtained by analytical expression 4.30 and the result discussed in Sec. 2.3.2, obtained by finite

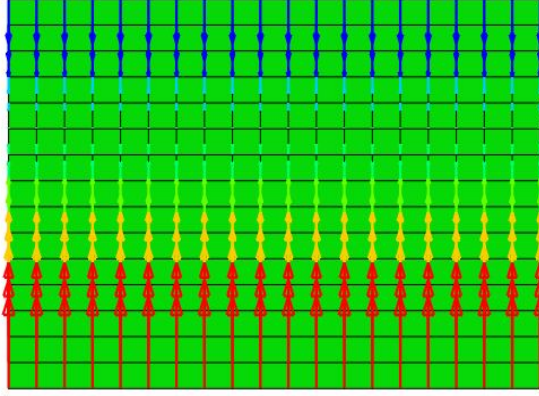


Figure 5.7:  $U_2$  displacement vectors for a model with boundary conditions given in Fig. 5.6. The red and blue arrows shows the direction of the displacement.

element based Monte Carlo simulations.

$$\frac{\sigma_{pl}}{\sigma_{ys}} = C\rho^n \quad (5.2)$$

We can find constants  $C$  and  $n$  by the methodology discussed in Sec. 3.1 using schematic shown in Fig. 3.1.

$$\ln\left(\frac{\sigma_{ly}}{\sigma_y}\right) = \ln C + n \ln \bar{\rho} \quad (5.3)$$

Relation of plastic collapse strength for the re-entrant hexagonal auxetic cell under consideration as given below

$$\frac{\sigma_{pl}}{\sigma_{ys}} = 0.467\rho^2 \quad (Theoretical) \quad (5.4)$$

$$\frac{\sigma_{pl}}{\sigma_{ys}} = 0.407\rho^{1.75} \quad (FE\ modelling) \quad (5.5)$$

Cellular solid typically have low relative density ( $\bar{\rho} \leq 0.2$ ). Analytical expression gives collapse strength same as FE simulations with acceptable error of maximum 12% for cellular solids.

## 5.2 Corner Singularity of Re-entrant Wedge

The singularity associated with the wedge angle can be assessed from Fig. 5.10 for symmetric field whereas for anti-symmetric field the variation is shown in Fig. 5.11 using Eqs. 4.48 and 4.49, respectively.

Singularity for a re-entrant wedge with re-entrant angle ( $\theta$ )  $75^\circ$  for a symmetric field can be found out either by using plot in Fig. 5.10 or by exclusively solving the implicit Eq. 4.48 by putting value of  $\alpha$  (i.e.  $180-\theta$ ). RHS function in Eq. 4.48 varies as shown in Fig. w.r.t. singularity  $\lambda$  of re-entrant corner.

The data cursor point in Fig. 5.12 includes the roots of Eq. 4.48 for re-entrant wedge. The

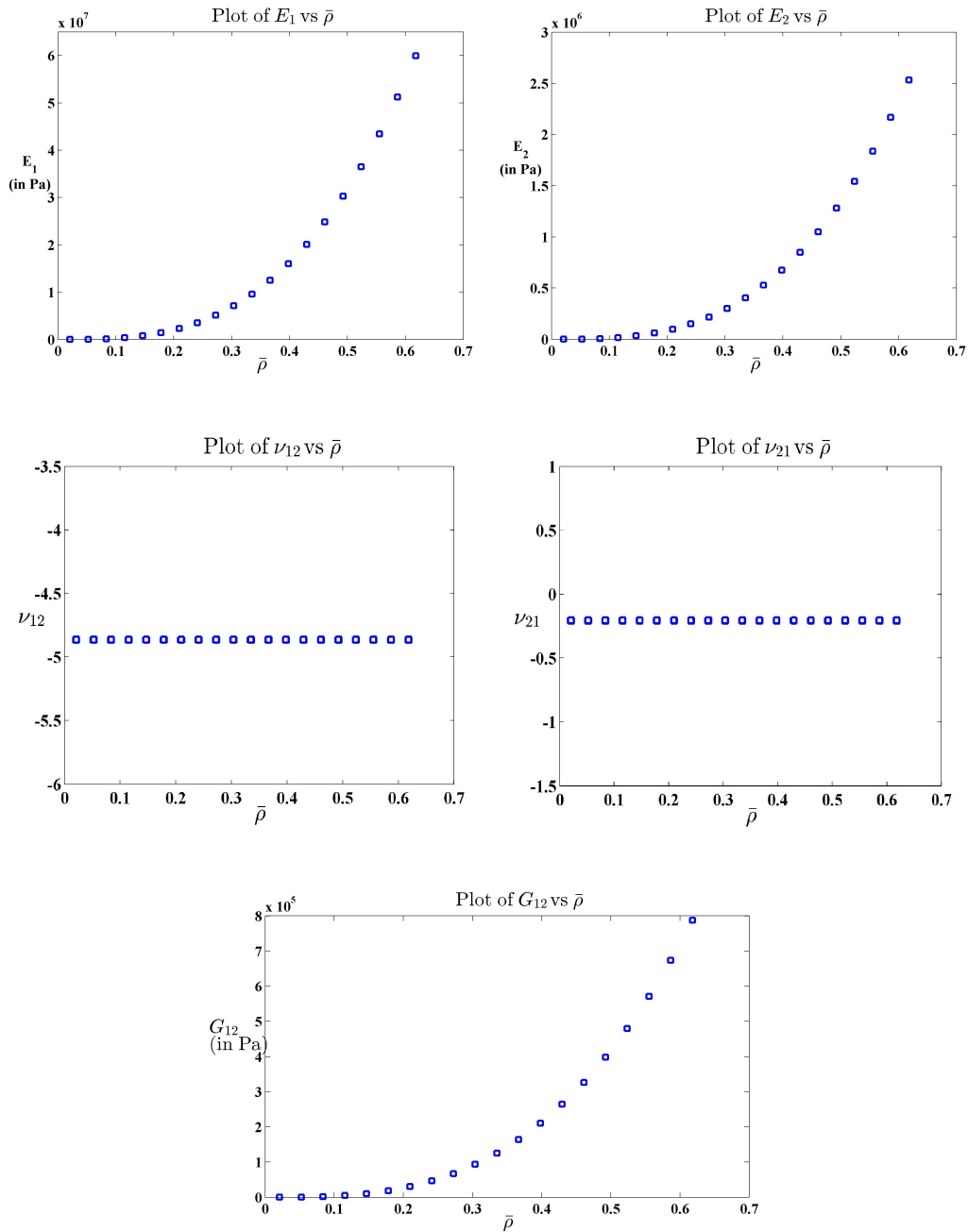


Figure 5.8: Variation of generalized elastic constants w.r.t. cell relative density of re-entrant hexagonal auxetics

eigenvalue value ( $\lambda$ ) is 0.75. As this study was intended to establish re-entrant hexagonal element for finite element calculations, corner singularity of it is a crucial step to proceed further. Extended finite element methods can be used to enrich the shape function of a rectangular 4-noded (or higher number of nodes) element such that it behaves as re-entrant hexagonal element. This method uses mainly corner singularity and heavy side function. It opens the door of future scope for this research.

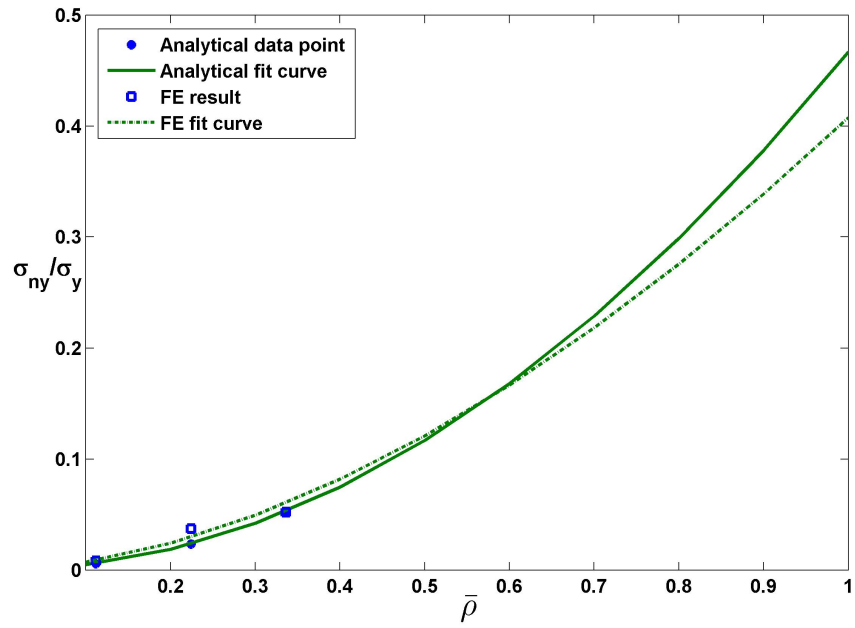


Figure 5.9: Comparison of theoretical plastic collapse strength and plastic collapse strength obtained by FE analysis

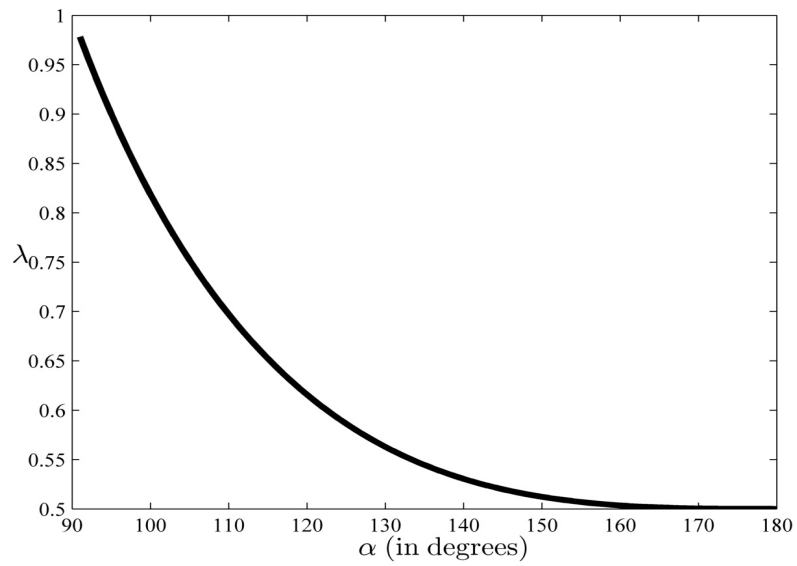


Figure 5.10: Eigenvalue for symmetric field w.r.t. wedge angle in symmetric field

### 5.3 Direct Stiffness Method using frame element

Coordinates of the nodes for the re-entrant hexagon unit cell with  $\frac{W}{h} = 1$  and  $\theta = 75^\circ$  in Fig. 4.9 are

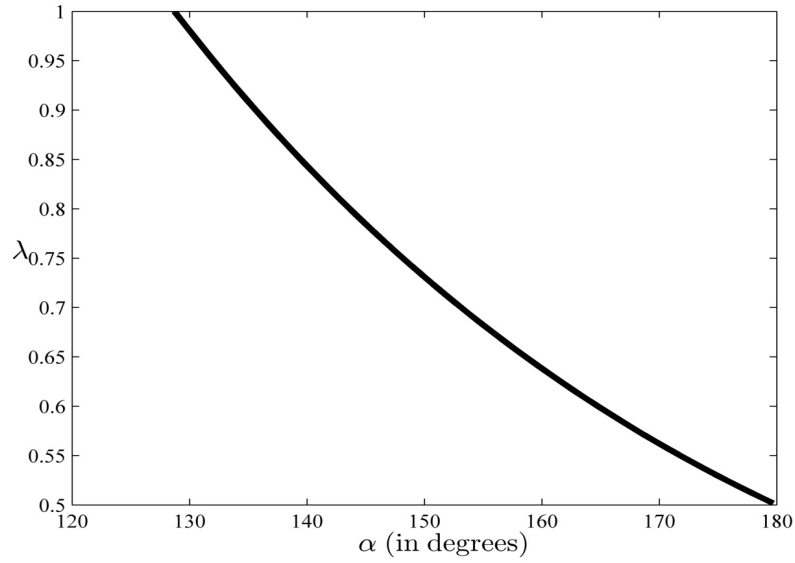


Figure 5.11: Eigen values for anti-symmetric field w.r.t. wedge angle in anti-symmetric field

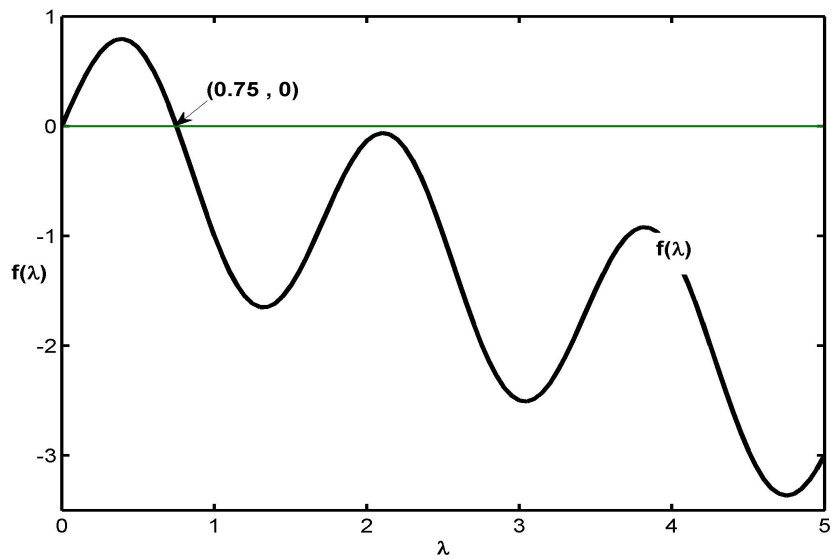


Figure 5.12: Eigen values for re-entrant corner ( $\alpha = 75^\circ$ ) in symmetric field

Node Number	X Coordinate	Y Coordinate
1	0.2411	0
2	0.5	0.966
3	-0.5	0.966
4	-0.2411	0
5	-0.5	-0.966
6	0.5	-0.966



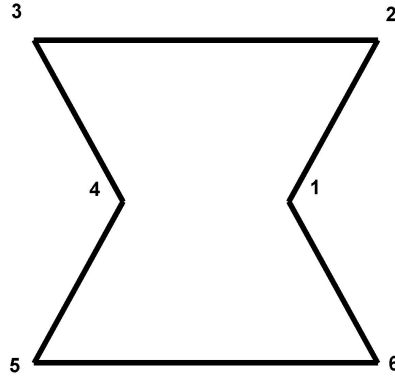


Figure 5.13: Re-entrant hexagon auxetic element node numbering

Global stiffness matrix for the re-entrant hexagon for given nodes can be found out by assembling the stiffness matrix of individual frames. According to Drucker's stability criteria eigen value of stiffness must be positive.

Eigen values of the re-entrant hexagon stiffness matrix are as given in the following table

Table 5.1: Eigen values of re-entrant hexagonal element stiffness obtained by direct stiffness method

0.00	0.00	0.00	17.05	23.48	25.82	39.99	59.27	119.99
133.66	149.59	204.02	359.94	359.97	400.68	442.89	500.41	522.82

Eigenvalues in the Tab. 5.1 are semi-positive which means that the re-entrant hexagonal auxetic ( $\theta = 75^\circ$ ) satisfies **Drucker stability** criteria which says that "eigenvalues of the elastic stiffness and compliance matrices must all be greater than zero". The first three zero eigenvalue are because of the unconstrained structure. The number of zeros for an unconstrained structure would be equal to the no. of degree of freedom each node possess.

## 5.4 Configurational Forces in Re-entrant Hexagonal Auxetic

Configurational force in re-entrant hexagon auxetic at re-entrant corner w.r.t. configuration parameter  $l$  varies as shown in Fig. 5.14

As the distance  $l$  decreases magnitude of configuration force  $Q$  also decreases which imply that the pseudo force required to open up the re-entrant angle is higher if the distance  $l$  is more and decreases if the distance  $l$  decrease. Figure 5.14 shows that the stable configuration would be achieved when the re-entrant angle completely opens up (i.e.  $\theta = 90^\circ$ ).

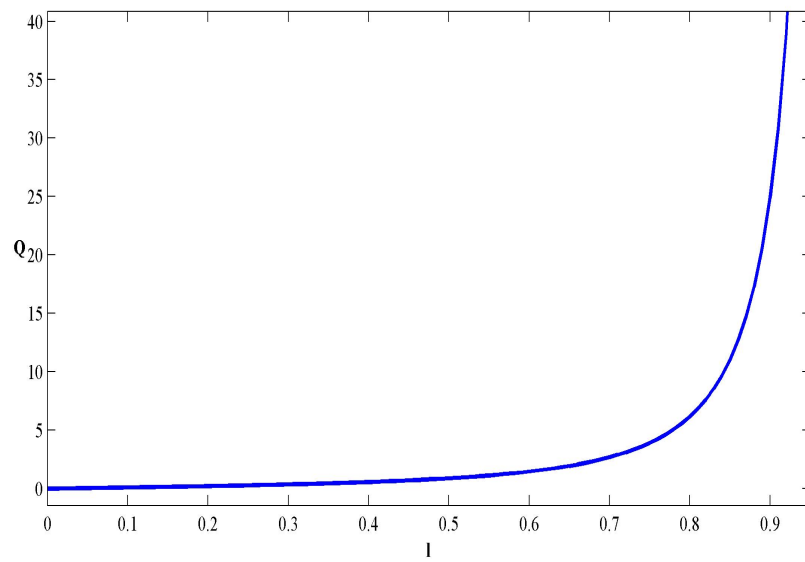


Figure 5.14: Variation of configurational force generated w.r.t.  $l$

# Chapter 6

## Conclusion and Future Scope

### 6.0.1 Key Conclusion

We have conducted two studies in this thesis. The first study is to estimate the blast resistance of sandwich structures comprising an auxetic core. Second study is to formulate a new enriched auxetic element by getting familiar with its micro-mechanics.

The first study shows that representative unit cell homogenization can be used for finding the equivalent longitudinal strength of the the cellular auxetic material. By implementing the three stage momentum transfer model we can obtain the design charts. These design charts can be used by the industries for designing the sandwich core panels. We have compared the blast resistance of different core topologies conventional as well as auxetics. We observed that re-entrant hexagonal auxetic core topology outperforms the other core topologies of sandwich core. However, in the analysis of auxetics the re-entrant angle has posed a huge computational requirement. And, this has motivated us to look for a better element. In second study we have studies the micro-mechanics of auxetics.

In this analysis we targeted to model an hourglass element ( double re-entrant solid element). In order to do that we found out the corner singularities. Using concept of extended finite element methods we attempted to enrich the shape function of 4-noded rectangular element with the corner singularities. We modelled re-entrant hexagonal auxetic using Ashby's beam column theory and elastic constant were found out. Plastic moment as function of micro-structural parameters of the re-entrant hexagonal auxetic was found out analytically using cellular material theory as given in Eq. 4.29. In next section direct stiffness matrix methods study concludes that re-entrant structure satisfies Drucker's stability criteria, implying that the configuration is stable. In the end, using configurational balance the pseudo force (i.e. configurational force) at the re-entrant corners was calculated. The variation of this pseudo force  $Q$  with the distance  $l$  implies that the most stable configuration is when the re-entrant angle is completely opened up (i.e.  $\theta = 90^\circ$ ).

### 6.0.2 Future Scope

In the future one can use Eshelby's equivalent inclusion theory in order to find the stable configuration and formulate the element. Difficult arises as the geometry of re-entrant hexagonal auxetic cell is irregular and complex. One can overcome to these difficult by using Schwartz christoffel transformation to transform re-entrant hexagonal strip to plate with a hole or any other simpler problem.

Superposition techniques also can be used in future in order to get stress distribution in the element using corner singularity calculated in this study by William's asymptotic solution. But the later technique would give solution for only  $r$  dominated region. So again Eshelby's equivalent approach could give the full fledged solution here.

## Appendix A

# Analytical Three Stage Momentum Transfer Model

This appendix includes a descriptive discussion about the analytical model for structural response of a sandwich beam to Blast loading proposed by Fleck and Deshpande [8].

### A.1 Model Description

As discussed earlier in Sec. 2.3.4, the structural response of the sandwich beam is split into a succession of three stages based on the significant time periods observed in these three distinct stages. The sandwich beam schematic is shown in Fig. A.1.

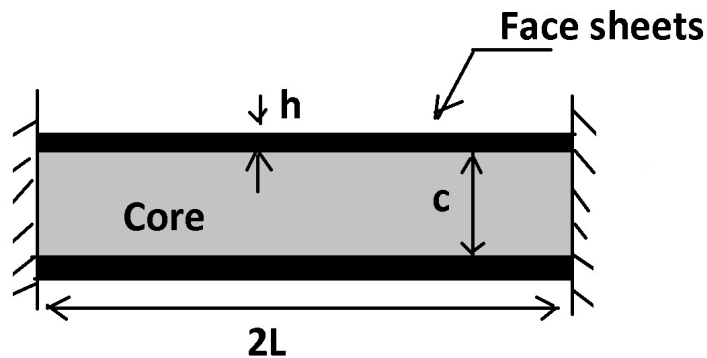


Figure A.1: Sandwich beam geometry

#### A.1.1 Stage I: One Dimensional Fluid-Structure Interaction Model.

Shock wave have been idealized as a planar wave falling normally and uniformly over the top face sheet. Variation of overall pressure magnitude could be mainly because of incoming pressure wave, reflection wave and rarefaction wave magnitudes. The net pressure on the front face sheet can be

given by

$$P(x, t) = P_I + P_{r1} + P_{r2} = P_o[e^{-(t+x/c_w)/\theta} + e^{-(t-x/c_w)/\theta}] + \rho_w c_w \dot{w}(t + \frac{x}{c_w}) \quad (\text{A.1})$$

Where  $P_I, P_{r1}, P_{r2}$  are incoming pressure wave, reflection wave and rarefaction wave magnitudes respectively. Here a typical assumption of a blast wave of exponential shape have been made having  $P_o$  as the peak pressure and  $\theta$  as the time decay constant. The origin is taken at the front face sheet of the sandwich panel.

The pressure distribution on the front face sheet (at  $x=0$ ) from Eq. A.1 is

$$p(t, x = 0) = 2p_o e^{-t/\theta} - \frac{2p_o \psi}{\psi - 1} [e^{-t/\theta} - e^{-\psi t/\theta}] \quad (\text{A.2})$$

Cavitation  $p(t, x = 0) \rightarrow 0$  occurs in a medium containing dissolved gases at time  $\tau_c$  which is called the cavitation time. From Eq. A.2 we get

$$\frac{\tau_c}{\theta} = \frac{1}{\psi - 1} \ln \psi \quad (\text{A.3})$$

and the impulse transferred to the front sheet is taken as

$$I_{trans} = \zeta I \quad (\text{A.4})$$

where

$$\zeta = \psi^{-\frac{\psi}{\psi-1}} \quad (\text{A.5})$$

and  $I$  is the maximum achievable blast impulse, defined as

$$I = \int_0^{\infty} 2p_o e^{-t/\theta} dt = 2p_o \theta \quad (\text{A.6})$$

The velocity  $v_o$  induced in the front face sheet is calculated by the definition of impulse as follows

$$v_o = \frac{I_{trans}}{m_f} \quad (\text{A.7})$$

### A.1.2 Stage II: One Dimensional Model of Core Compression Phase

In the second stage, the core gets crushed due to the velocity attained in the front face sheet from the stage I and consequently, the core and rear face sheet accelerates while the front face sheet gets decelerated. The core is treated rigid, ideally plastic crushable solid having nominal compressive strength  $\sigma_{ny}$  up to a nominal densification strain. The core is treated rigid, after the densification strain is achieved. The energy and momentum conservation is used in order to determine the value of core compressive strain  $\epsilon_c$  ( $\leq \epsilon_D$ ) and the final velocity,  $v_f$ , achieved in face and core at the end of the crushing stage. Momentum conservation in the core core crush phase given that

$$(2m_f + \rho_c c) v_f = m_f v_o \quad (\text{A.8})$$

The ratio of the energy lost  $U_{lost}$  in the core crushing to the initial kinetic energy is given by

$$\frac{U_{lost}}{m_f v_o^2 / 2} = \frac{1 + \hat{\rho}}{2 + \hat{\rho}} \quad (\text{A.9})$$

where  $\hat{\rho} = \frac{\rho_c c}{m_f}$ . This energy is lost because of plastic dissipation in the core crushing, we can represent it as

$$U_{lost} = \sigma_{ny} \epsilon_c c \quad (\text{A.10})$$

where  $\epsilon_c$  is the compressive strain in the core. Using Eq. A.9 and Eq. A.10, the compressive strain  $\epsilon_c$  is given as

$$\epsilon_c = \frac{\epsilon_D}{2} \frac{1 + \hat{\rho}}{2 + \hat{\rho}} \hat{I}^2 \quad (\text{A.11})$$

where  $\hat{I}$  is a non-dimensional parameter given as

$$\hat{I} = \frac{I_{trans}}{\sqrt{m_f c \sigma_{ny} \epsilon_c}} \quad (\text{A.12})$$

If the  $U_{lost}$  is too high such that the compressive strain  $\epsilon_c$  exceeds the densification strain  $\epsilon_D$  then  $\epsilon_c$  is taken equal to the value of  $\epsilon_D$  and additional dissipation must occur using different mechanisms. This analysis neglects these additional mechanisms.

### A.1.3 Stage III: Dynamic Structural Response of Clamped Sandwich Beam

At the end of Stage II the rear face sheet achieves a uniform velocity  $v_f$  as given in Eq. A.8. This final stage includes the dissipation of kinetic energy acquired in stage I and stage II by beam bending and longitudinal stretching. This turn out to be a classical problem: What is the dynamic response of a clamped beam of length  $2L$  made up of rigid ideally plastic material with mass per unit length  $m$  subjected to an initial velocity  $v_f$  in the transverse direction. This stage is divided in two phases. Phase I includes the plastic hinge formation in the beam and continues until the hinges coalesce at the center. In Phase II: the beam behaves as a strings and starts vibrating.

Plastic hinge is formed at the ends in order to remove the indeterminacy of the structure. The plastic hinges then travels towards the center, towards the ends of the beam as shown in Fig. A.2. Conservation angular momentum about a fixed end after a time  $t$  for the clamped beam gives

$$(mLv_f) \frac{L}{2} = m(L - \xi)v_f \left( \xi + \frac{L - \xi}{2} \right) + 2M_o t + \frac{1}{2} N_o v_f t^2 + \int \frac{mv_f x^2}{\xi} dx \quad (\text{A.13})$$

where  $x$  is the axial coordinate from the end of the beam as shown in Fig. A.2(b). From Eq. A.13,  $\xi$  as a function of time  $t$  comes as

$$\xi = \sqrt{\frac{3t(v_f N_o t + 4M_o)}{mv_f}} \quad (\text{A.14})$$

where  $M_o$  and  $N_o$  are plastic moment and plastic force of for the sandwich beam, respectively.

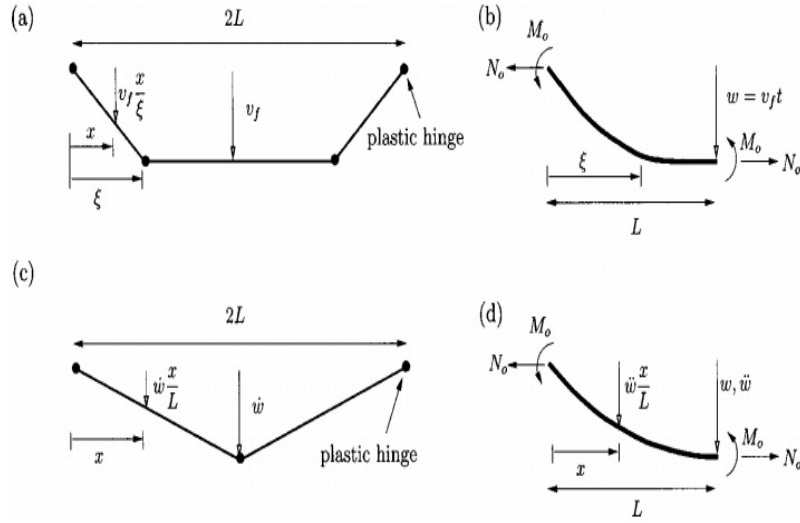


Figure A.2: Plastic hinges formation in Stage III

Time period of Phase I is the time taken by the plastic hinges to travel from ends to the midspan, i.e. when  $\xi = L$ . Using Eq. A.14, the time period,  $T_1$ , for the phase I is given as

$$T_1 = \frac{M_o}{N_o v_f} \left[ \sqrt{\frac{mL^2 v_f^2 N_o}{3M_o^2}} - 2 \right] \quad (\text{A.15})$$

and the displacement  $w_1$  of the mid point can be given as

$$w_1 = v_f T_1 \quad (\text{A.16})$$

$$\implies \frac{M_o}{N_o} \left[ \sqrt{\frac{mL^2 v_f^2 N_o}{3M_o^2}} - 2 \right] \quad (\text{A.17})$$

In phase II, the beam behaves at a stretched beam and the velocity profile is triangular as sketched in Fig. A.2(c). Equation of motion for half beam in phase II can be formulated from Fig. A.2(d) as

$$\begin{aligned} 2M_o + N_o w &= -\frac{\ddot{w}}{L} \int_0^L m x^2 dx \\ &\implies -\frac{mL^2}{3} \ddot{w} \end{aligned} \quad (\text{A.18})$$

With initial conditions  $w(T_1) = w_1$  and  $\dot{w}(T_1) = v_f$ , the solution of the differential Eq. A.18 is

$$w(t) = \frac{v_f}{\omega} \sin[\omega(t - T_1)] + \left( \frac{2M_o}{N_o} + w_1 \right) \cos[\omega(t - T_1)] - \frac{2M_o}{N_o} \quad (\text{A.19})$$



where

$$\omega = \frac{1}{L} \sqrt{\frac{3N_o}{m}} \quad (\text{A.20})$$

The beam has an harmonic motion following the Eq. A.19. The maximum deflection  $w_{max}$  of the mid point at time  $T$  is obtained as

$$w_{max} = \sqrt{\frac{v_f^2}{\omega^2} + \left(\frac{2M_o}{N_o} + w_1\right)^2} - \frac{2M_o}{N_o} \quad (\text{A.21})$$

and the time period  $T$  is

$$T = T_1 + \frac{1}{\omega} \tan^{-1} \left[ \frac{N_o v_f}{\omega(2M_o + w_1 N_o)} \right] \quad (\text{A.22})$$

The plastic bending moment of a sandwich beam is given by

$$M_o = \sigma_{ly} \frac{(1 - \epsilon)^2 c^2}{4} + \sigma_{fy} h [(1 - \epsilon_c + h)] \quad (\text{A.23})$$

whereas, the plastic membrane force  $N_o$  is given as (assuming that it will not be affected by the degree of core compression)

$$N_o = 2\sigma_{fy} h + \sigma_{ly} c \quad (\text{A.24})$$

The non-dimensional parameters is used in constructing the generalized design charts. Non-dimensional geometric parameters are

$$\bar{c} \equiv \frac{c}{L}, \quad \bar{h} \equiv \frac{h}{L} \quad (\text{A.25})$$

and non-dimensional relative density is

$$\bar{\rho} \equiv \frac{\rho_c}{\rho_f} \quad (\text{A.26})$$

The non-dimensional time response ( $\bar{T}$ ) and impulse ( $\bar{I}$ ) are given by

$$\bar{T} \equiv \frac{T}{L} \sqrt{\frac{\sigma_{fy}}{\rho_f}}, \quad \bar{I} \equiv \frac{I}{L \sqrt{\rho_f \sigma_{fy}}} \quad (\text{A.27})$$

# References

- [1] T.-C. Lim. *Auxetic Materials and Structures (Engineering Materials)*. Springer, 2014.
- [2] P. Aldred and S. C. Moratti. Dynamic simulations of potentially auxetic liquid-crystalline polymers incorporating swivelling mesogens. *Molecular Simulation* 31, (2005) 883–887.
- [3] J. Dirrenberger, S. Forest, D. Jeulin, and C. Colin. Homogenization of periodic auxetic materials. *Procedia Engineering* 10, (2011) 1847–1852.
- [4] J. Wang, R. Wagoner, D. Matlock, and F. Barlat. Anticlastic curvature in draw-bend springback. *International Journal of Solids and Structures* 42, (2005) 1287–1307.
- [5] Lakes and Roderic. Foam structures with a negative Poisson’s ratio. *Science* 235, (1987) 1038–1040.
- [6] R. Critchley, I. Corni, J. A. Wharton, F. C. Walsh, R. J. K. Wood, and K. R. Stokes. The Preparation of Auxetic Foams by Three-Dimensional Printing and Their Characteristics. *Advanced Engineering Materials* .
- [7] A. Alderson. A triumph of lateral thought. *Chem. Ind* 10, (1999) 384.
- [8] Fleck NA and Deshpande VS. The resistance of clamped sandwich beams to shock loading. *Journal of Applied Mechanics* 71, (2004) 386–401.
- [9] Young T. On passive strength and friction. *Course of lectures on natural philosophy and the mechanical arts: lecture* 13, (1807) 109–113.
- [10] Poisson SD. Note sur l’extension des fils et des plaques élastiques. *Annales de Chimie et de Physique* 36, (1827) 384–387.
- [11] G. Kirchhoff. Ueber das Verhältniss der Quercontraction zur Längendilatation bei Stäben von federhartem Stahl. *Annalen der Physik* 184, (1859) 369–392.
- [12] Cauchy AL. Sur les équations qui expriment les conditions d’équilibre ou les lois du mouvement intérieur d’un corps solide, élastique ou non élastique. *Exercices de Mathématiques* 3, (1828) 160–187.
- [13] Y. Prawoto. Seeing auxetic materials from the mechanics point of view: A structural review on the negative Poisson’s ratio .
- [14] Lakes RS and Elms K. Indentability of conventional and negative Poisson’s ratio foams. *Journal of Composite Materials* 27, (1993) 1193–1202.

- [15] Choi JB and Lakes RS. Fracture toughness of re-entrant foam materials with a negative Poisson's ratio: experiment and analysis. *International Journal of Fracture* 80, (1996) 73–83.
- [16] Huang X and Blackburn S. Developing a New Processing Route to Manufacture Honeycomb Ceramics with Negative Poisson's Ratio. *Key Engineering Materials* 213.
- [17] K.L. Alderson, A.P. Pickles, P.J. Neale, and K.E. Evans. Auxetic polyethylene: The effect of a negative poisson's ratio on hardness. *Acta Metallurgica et Materialia* 42, (1994) 2261 – 2266.
- [18] Lipsett A William and Beltzer Abraham I. Reexamination of dynamic problems of elasticity for negative Poisson's ratio. *The Journal of the Acoustical Society of America* 84, (1988) 2179–2186.
- [19] K. E. Evans and A. Alderson. Auxetic materials: functional materials and structures from lateral thinking! *Advanced materials* 12, (2000) 617–628.
- [20] KE Evans. The design of doubly curved sandwich panels with honeycomb cores. *Composite Structures* 17, (1991) 95–111.
- [21] Greaves G.N., Greer A.L., Lakes R.S., and Rouxel T. Poisson's ratio and modern materials. *Nature Materials* 10, (2011) 823–837.
- [22] G. N. Greaves. Poisson's ratio over two centuries: challenging hypotheses. *Notes and Records of the Royal Society* 67, (2013) 37–58.
- [23] Y. C. Fung. *Foundations of Solid Mechanics (International Series in Dynamics)*. Prentice Hall, 1965.
- [24] A. Yeganeh-Haeri, D. J. Weidner, and J. B. Parise. Elasticity of  $\alpha$ -Cristobalite: A Silicon Dioxide with a Negative Poisson's Ratio. *Science* 257, (1992) 650–652.
- [25] H. Kimizuka, S. Ogata, and Y. Shibutani. High-Pressure Elasticity and Auxetic Property of  $\alpha$ -Cristobalite. *MATERIALS TRANSACTIONS* 46, (2005) 1161–1166.
- [26] N. R. Keskar and J. R. Chelikowsky. Negative Poisson ratios in crystalline SiO<sub>2</sub> from first-principles calculations. *Nature* 358, (1992) 222–224.
- [27] C. He, P. Liu, P. J. McMullan, and A. C. Griffin. Toward molecular auxetics: Main chain liquid crystalline polymers consisting of laterally attached para-quaterphenyls. *physica status solidi (b)* 242, (2005) 576–584.
- [28] L. Jinhee, C. JB, and C. K. Application of homogenization FEM analysis to regular and re-entrant honeycomb structures. *Journal of Materials Science* 31, (1996) 4105–4110.
- [29] Fozdar David Y, Soman Pranav, Lee Jin Woo, Han Li-Hsin, and Chen Shaochen. Three-Dimensional Polymer Constructs Exhibiting a Tunable Negative Poisson's Ratio. *Advanced functional materials* 21, (2011) 2712–2720.
- [30] Gibson LJ and Ashby MF, Schajer GS, and Robertson CI. The mechanics of two-dimensional cellular materials. *Proceedings of the Royal Society of London. A. Mathematical and Physical Sciences* 382, (1982) 25–42.

- [31] Kolpakov AG. On the determination of the averaged moduli of elastic gridworks. *Prikl. Mat. Mekh* 59, (1985) 969–977.
- [32] Lorna J. Gibson and Michael F. Ashby. Cellular Solids-Structure and Properties. 2nd edition. Cambridge University Press, New York, 1997.
- [33] Yang DU, Lee S, and Huang FY. Geometric effects on micropolar elastic honeycomb structure with negative Poisson’s ratio using the finite element method. *Finite elements in analysis and design* 39, (2003) 187–205.
- [34] Gonella Stefano and Ruzzene Massimo. Homogenization and equivalent in-plane properties of two-dimensional periodic lattices. *International Journal of Solids and Structures* 45, (2008) 2897–2915.
- [35] Donescu Stefania, Chiroiu Veturia, and Munteanu Ligia. On the Young’s modulus of a auxetic composite structure. *Mechanics Research Communications* 36, (2009) 294–301.
- [36] Friis EA, Lakes RS, and Park JB. Negative Poisson’s ratio polymeric and metallic foams. *Journal of Materials Science* 23, (1988) 4406–4414.
- [37] N Chan and K E Evans. Fabrication methods for auxetic foams. *Journal of Materials Science* 32.
- [38] M. M. Swisdak. Explosion Effects and Properties-Part II: Explosion Effects in Water. Technical Report, Naval Surface Weapons Center, Research and Technology Department 1978.
- [39] R. H. Cole and R. Weller. Underwater Explosions. *Physics Today* 1, (1948) 35.
- [40] M. Ashby, A. Evans, N. Fleck, L. Gibson, J. Hutchinson, and H. Wadley. Metal foams: a design guide. butterworth-heinemann, 2000.
- [41] W. Miller, C. Smith, and K. Evans. Honeycomb cores with enhanced buckling strength. *Composite Structures* 93, (2011) 1072–1077.
- [42] K. P. Dharmasena, H. N. Wadley, Z. Xue, and J. W. Hutchinson. Mechanical response of metallic honeycomb sandwich panel structures to high-intensity dynamic loading. *International Journal of Impact Engineering* 35, (2008) 1063–1074.
- [43] F. Zhu, L. Zhao, G. Lu, and Z. Wang. Deformation and failure of blast-loaded metallic sandwich panels - Experimental investigations. *International Journal of Impact Engineering* 35, (2008) 937–951.
- [44] G. Nurick, G. Langdon, Y. Chi, and N. Jacob. Behaviour of sandwich panels subjected to intense air blast – Part 1: Experiments. *Composite Structures* 91, (2009) 433–441.
- [45] D. Radford, G. McShane, V. Deshpande, and N. Fleck. The response of clamped sandwich plates with metallic foam cores to simulated blast loading. *International Journal of Solids and Structures* 43, (2006) 2243–2259.

- [46] G. McShane, D. Radford, V. Deshpande, and N. Fleck. The response of clamped sandwich plates with lattice cores subjected to shock loading. *European Journal of Mechanics - A/Solids* 25, (2006) 215–229.
- [47] E. Wang, N. Gardner, and A. Shukla. The blast resistance of sandwich composites with stepwise graded cores. *International Journal of Solids and Structures* 46, (2009) 3492–3502.
- [48] Z. Xue and J. W. Hutchinson. A comparative study of impulse-resistant metal sandwich plates. *International Journal of Impact Engineering* 30, (2004) 1283–1305.
- [49] Wei Yang, Zhong-Ming Li, Wei Shi, Bang-Hu Xie, and Ming-Bo Yan. Review on auxetic materials. *Journal of Materials Science* 39, (2004) 3269–3279.
- [50] F Cote, VS Deshpande, NA Fleck, and AG Evans. The out-of-plane compressive behaviour of metallic honeycombs. *Materials Science and Engineering* 380, (2004) 272 – 280.
- [51] Wicks, Nathan, Hutchinson, and John W. Performance of sandwich plates with truss cores. *Mechanics of Materials* 8, (2004) 739–751.
- [52] L. Valdevit, J.W. Hutchinson, and A.G. Evans. Structurally optimized sandwich panels with prismatic cores. *International Journal of Solids and Structures* 41, (2004) 5105 – 5124.
- [53] Evans KE, Nkansah MA, Hutchinson IJ, and Rogers SC. Molecular network design. *Nature* 353, (1991) 124–124.
- [54] Prall D and Lakes RS. Properties of a chiral honeycomb with a Poisson’s ratio of  $\tilde{\nu} = -1$ . *International Journal of Mechanical Sciences* 39, (1997) 305–314.
- [55] F. Robert. An isotropic three-dimensional structure with Poisson’s ratio  $-1$ . *Journal of Elasticity* 15, (1985) 427–430.
- [56] Norman Jones. *Structural Impact*. 2nd edition. Cambridge University Press, New York, 2012.
- [57] Symmonds P. S. Large Plastic Deformations of Beams Under Blast Type Loading. In Second U.S. National Congress of Applied Mechanics. 1954 505–515.
- [58] E. Achenbach. Response of a solid oxide fuel cell to load change. *J. Power Sources* 57, (1995) 105–109.
- [59] J. D. Eshelby. The Determination of the Elastic Field of an Ellipsoidal Inclusion, and Related Problems. *Proceedings of the Royal Society A: Mathematical, Physical and Engineering Sciences* 241, (1957) 376–396.
- [60] J. D. Eshelby. The Force on an Elastic Singularity. *Philosophical Transactions of the Royal Society A: Mathematical, Physical and Engineering Sciences* 244, (1951) 87–112.